3

Force Spectroscopy on Semiconductor Surfaces

Oscar Custance, Noriaki Oyabu, and Yoshiaki Sugimoto

Abstract. In this chapter, we introduce recent works on force spectroscopy performed using the frequency modulation detection method that have contributed to widen the knowledge and applicability of atomic force microscopy (AFM) for the study of surfaces with atomic resolution. We first introduce some experimental considerations regarding force spectroscopy acquisition. Then, we discuss how the combination force spectroscopy and first-principle calculations has contributed to clearly identify a channel for the dissipation of energy from the cantilever oscillation, as well as to clarify the interplay between atomic relaxations and differences in the tip–surface short-range interaction detected over atoms populating heterogeneous semiconductor surfaces. We introduce a protocol for single-atom chemical identification using AFM, which is based on the precise quantification of the tip–surface short-range interaction forces. Finally, anticipating the future general use of small cantilever oscillation amplitudes, we discuss force spectroscopy acquisition using higher flexural modes of rectangular cantilevers and oscillation amplitude values as small as 3.6 Å.

3.1 Introduction

Soon after its invention, the atomic force microscope (AFM) [1] demonstrated to be a very versatile tool for exploring and interacting with matter at the micro- and nanoscale, in different environments and with multiple applications in fields ranging from biology to semiconductor industry. Depending on the research field, the AFM is renamed as scanning force microscope, surface force microscope, and alike. However, the name selected by Binnig, Quate, and Gerber to succinctly refer to their invention [1] was probably chosen to stress that with this apparatus it could be possible to detect interatomic forces, and therefore, explore surfaces with true atomic resolution. It took almost a decade to beat all the technical adversities and demonstrate that AFM can certainly detect interatomic forces and obtain atomically resolved images of

S. Morita et al. (eds.), *Noncontact Atomic Force Microscopy*,
NanoScience and Technology,
DOI: 10.1007/978-3-642-01495-6_3, © Springer-Verlag Berlin Heidelberg 2009

highly reactive surfaces [2–4]. This breakthrough was in part possible, thanks to the development of the frequency modulation detection method by Albrecht and co-workers [5]. Since the achievement of true-atomic resolution with AFM, there was an increasing number of groups and researchers showing interest in frequency modulation atomic force microscopy (FM-AFM) not only for the study of conducting an insulating surfaces at the atomic scale, but for many other additional possibilities that this highly sensitive detection scheme offers to study different kind of phenomena at surface. There are excellent reviews that describe pioneering works in FM-AFM [6–8], that have instructed and inspired new generations of researchers excited by the possibilities offered by this technique.

Since the publication of these reviews, there has been significant progress in the field. One of the subjects that has undertaken an extraordinary development in recent years is force spectroscopy, which is the technique that allows us to quantify very precisely the tip–surface interaction forces exerted on the cantilever. In FM-AFM, these forces are indirectly obtained from variations of the cantilever resonant frequency as the tip–surface distance is continuously explored.

One of the first attempts to quantify the tip–surface interaction force as a function of the tip–surface distance in FM-AFM was performed by Gotsmann and co-workers [9–11]. Almost at the same time, important contributions were also performed by the group at Hamburg University [12–15]. However, it was the group of Basel University the one who achieved the breakthrough of quantifying the short-range forces associated with a single bond formation between the outermost atom of the tip and the atoms probed at the surface [16]. These pioneering works inspired and encouraged us to implement and make use of force spectroscopy in our AFM experiments.

In this chapter, we will introduce recent works on force spectroscopy performed on semiconductor surfaces, which have contributed to widen our knowledge on phenomenology of FM-AFM and have broaden the applicability of AFM for the study of surfaces with atomic resolution. We will first introduce some experimental considerations regarding force spectroscopy acquisition. Then, we will discuss how the combination force spectroscopic measurements and first-principle calculations has contributed to clearly identify a channel for the dissipation of energy from the cantilever oscillation, as well as the interplay between atomic relaxations and differences in the tip–surface short-range interaction of atoms populating heterogeneous semiconductor surfaces. We will introduce a protocol for single-atom chemical identification using AFM based on the precise quantification of the tip–surface short-range interaction forces. And finally, anticipating the future general use of small cantilever oscillation amplitudes, we will discuss force spectroscopy acquisition using higher flexural modes of rectangular cantilevers and oscillation amplitude values as small as 3.6 Å.

3.2 Experimental Considerations

In FM-AFM, the cantilever is constantly excited at resonance keeping the oscillation amplitude constant. In this detection scheme, the main observable is the frequency shift: the variation of the cantilever resonant frequency with respect to the free oscillation value upon the presence of an inhomogeneous force field between the cantilever tip and the surface.

Scanning the surface maintaining constant a frequency shift value chosen as image set point gives access to topographic maps of the surface, when properly adjusting the feedback parameters to obtain a minimal error in the frequency shift signal with respect to the set point value. It is convenient to record in every moment the cantilever oscillation amplitude – to corroborate that it is kept constant – and the excitation signal applied to the piezo actuator that drives the cantilever oscillation (which is related to the additional amount of energy one has to put into the cantilever oscillation to keep the oscillation amplitude constant under the presence of nonconservative tip–surface interaction, see Sect. 3.3 for more details).

Atomic resolution experiments normally require operation of the AFM in ultrahigh vacuum (UHV) environment. In UHV, the common forces sensed by the cantilever tip are the electrostatic interaction due to the presence of a charge difference between tip and surface; the van der Waals interaction, which is originated by dipole fluctuations at tip and surface; and the short-range forces between the closest tip–surface atoms responsible of atomic contrast [17–19]. For magnetic tips or surfaces, there may be also magnetic forces involved even at atomic level [20]. To maximize sensitivity to the short-range forces, a bias voltage between tip and sample is normally applied to cancel the tip–surface contact potential difference to minimize the long-range electrostatic interaction [21, 22], and cantilevers with sharp tips at their free end – tips with typical radius of a few nanometers – are used to reduce the van der Waals contribution to the total interaction force.

Sharp yet atomically reactive tips are required to explore semiconductor surfaces. To this end, prior the experiments, it is convenient to prepare a new cantilever tip by ion Ar sputtering. We use an ion energy of $\sim$0.6 keV for our Si cantilevers, adjusting the partial pressure of Ar to get a typical ion current of $\sim$0.2 μA measured at the cantilever holder, setting the sputter time to obtain reactive yet sharp tips giving high quality atomic resolution images (the sputter time must be recalibrated for a given cantilever wafer). Sometimes, gentle contacts with the surface are required to improve atomic resolution image quality or to stabilize the tip apex after unintended modifications during scanning or force spectroscopy measurements. If the tip is producing stable imaging and good force spectroscopy data, it can be used over several measurement sessions without any further cleaning treatment.

When using cantilevers and a detection system based on optical interferometry, higher sensitivity is obtained by positioning the laser spot as close as possible to the cantilever-free end, while keeping a good and stable oscillation

signal coming out from the interferometer and the frequency demodulator. This optimum positioning of the laser spot can be easily performed by looking at the diffraction patterns provided by the output signal from the interferometer when longitudinally and transversally scanning the laser spot over the cantilever-free end. This requires a system of piezoelectric motors capable of moving the laser spot in three dimensions [23].

Site-specific force spectroscopy is performed by recording the frequency shift signal over a surface atomic site while decreasing the relative tip–sample distance. It is convenient to explore a distance range from the free oscillation region (absence of any force exerted on the cantilever) to distances beyond the onset of significant short-range interaction responsible of atomic contrast [17–19]. A set of forward and backward curves is usually acquired upon approach (retraction) of the tip towards (from) the surface and, under normal acquisition conditions, the curve upon retraction should match – within the experimental noise – the one acquired during the approach. After the acquisition of force spectroscopic characteristics, the surface should be imaged to assure that neither the tip nor the surface has changed. High degree of precision and reproducibility in positioning the tip over the top most part of a surface atom at both cryogenic and ambient temperatures can be achieved by using the atom tracking technique [24, 25]. In UHV experiments at room temperature, this tool can also be applied for the prediction and compensation of constant thermal drift in the three spatial dimensions [26] (for more details see Chap. 2).

3.2.1 Extraction of the Short-Range Force from the Frequency Shift

In FM-AFM, the frequency shift is proportional to a weighted average of the tip–surface interaction force over one cantilever oscillation cycle. For small enough perturbations of the harmonic behavior of the cantilever oscillation, the frequency shift (Δf) can be expressed as [14, 27, 28]

$$\Delta f = \frac{f_{\mathrm{r}}}{\pi k_{\mathrm{s}} A_0} \int_{-1}^{1} F_{\mathrm{int}}[z' + A_0(1+u)] \left(\frac{-u}{\sqrt{1-u^2}} \right) \mathrm{d}u, \tag{3.1}$$

(where f_{r} is the free-oscillation cantilever resonant frequency, k_{s} is the cantilever stiffness, A_0 is the cantilever oscillation amplitude, F_{int} is the tip–surface interaction force, and $z' = z - q$ is the tip–surface distance, with q being the generalized coordinate of the point-mass model that describes the harmonic oscillation of the tip [11, 14]). The kernel function

$$K(u) = \left(\frac{-u}{\sqrt{1-u^2}} \right) \quad u \in \{-1, 1\} \tag{3.2}$$

has important consequences when operating FM-AFM at either large or small oscillation amplitudes. For large oscillation amplitudes, this kernel assures

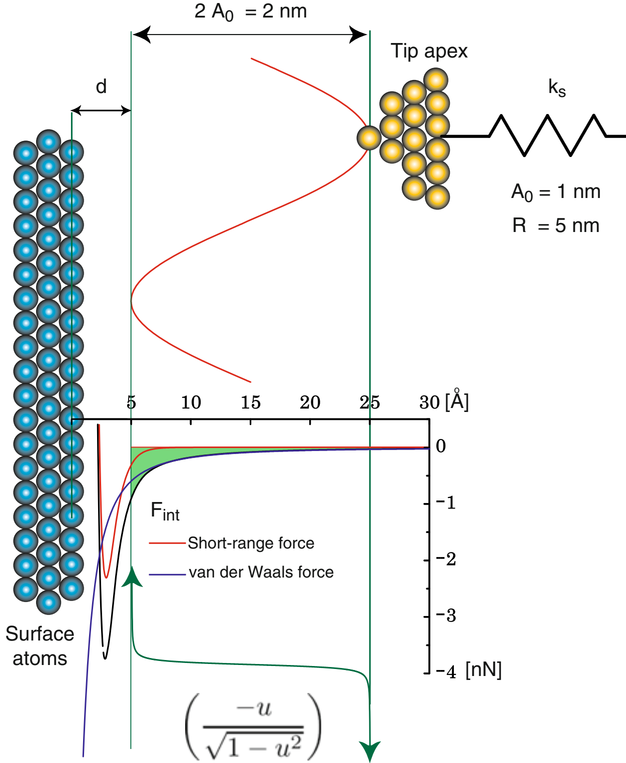

Fig. 3.1. A total interaction force (F_{int}) comprised by the short-range forces associated with a Si–Si interatomic interaction and the van der Waals force for a Si tip of 5 nm nominal radius. The behavior of the kernel function shown in (3.2) over a cantilever oscillation amplitude of 1 nm (total cantilever oscillation path of 2 nm) and a closest tip–surface distance approach (d) of 5 Å is also displayed

that the main contribution to the frequency shift comes from the point of closest proximity of the tip to the surface, as at the divergence for $u = 1$, the tip–surface interaction is normally negligible [28] (see Fig. 3.1). For small oscillation amplitudes, the kernel is responsible for the partial cancelation of the long-range interaction upon a small enough variation of these forces over a distance range equivalent to the total cantilever oscillation path [29, 30].

Force spectroscopy is based on (3.1), and obtaining the tip–surface interaction force from the measured frequency shift requires the inversion of this expression. This is, however, a nontrivial mathematical operation. Gotsmann [10], Durig [28], Giessibl [29], and Sader [31] have proposed different inversion procedures to obtain the tip–surface interaction force from (3.1). We have found that the methods proposed by Giessibl and Sader are more robust against the presence of experimental noise. While Giessibl's method requires powerful mathematical routines – commercially available – to invert a matrix

of $(n \times n)$ elements, with n the number of points of the frequency shift vs. tip–sample distance curve, the method proposed by Sader can be easily implemented having basic computational programing skills. Proper extraction of the tip–surface interaction force with Sader's method requires, however, exploring a tip–surface distance range extending to the free oscillation region; otherwise, the whole force curve will be shifted as a unit to smaller absolute force values. In cases where it is not possible to reach tip–surface distances entering in the free oscillation region, Giessibl's method may provide more accurate force values as the separation from the short-range interaction region is increased. In an overall evaluation, when reaching tip–sample distances corresponding to the free oscillation region, we have obtained a better performance using the method proposed by Sader and Jarvis [31]. The force extracted from frequency shift curves presenting significant instabilities loses its meaning as (3.1) is not well defined upon the presence of jumps in the frequency shift [14, 27, 32], and an alternative analysis is then required [33].

The tip–surface interaction forces extracted from the frequency shift vs. tip–sample distance curves include both long- and short-range interactions. The short-range forces can be obtained by subtracting the long-range contribution from the total force [22]. As during data acquisition the electrostatic force is minimized by compensating the tip–surface contact potential difference, the main long-range contribution comes from the van der Waals interaction. When possible, the long-range contribution should be characterized over surface sites not showing an apparent short-range interaction over a significant tip–surface distance range close enough to the surface, like, for example, over holes or vacancies [16, 24, 34]. In heterogeneous surfaces, upon the absence of surface sites for the direct characterization of the long-range interaction, it can be assumed that the long-range region embraces a distance from the free-oscillation regime to the position at which the total force curve for the different atomic species populating the surface starts deviating from a common behavior [35] (care about possible topographic offsets due to the acquisition protocol has to be taken [36], see Sect. 3.4 for details). An appropriate fitting of the total force over the long-range region to a Hamaker-like analytic model for the van der Waals interaction of a sphere over a plane [16] provides a good approximation to characterize the long-range contribution. Finally, the short-range interaction force is obtained by the subtraction of this fit evaluated over the whole tip–sample distance range explored to the total force curve.

3.2.2 Determination of Relevant Acquisition Parameters

The accuracy quantifying the tip–surface interaction force essentially depends on a proper characterization of the relevant acquisition parameters in FM-AFM. These are the cantilever oscillation amplitude, the cantilever stiffness, and the quality factor (Q) of the cantilever oscillation (in case that the

quantification of the energy dissipated from the cantilever would be also required).

The Q-value can be determined by the ring-down method, in which the excitation driving the cantilever at resonance is suddenly interrupted and the evolution of the square of the amplitude with time follows an exponential decay with a time constant given by $Q/2\pi f_0$, where f_0 is the cantilever resonant frequency. The Q-value can be also obtained from the width of the resonant peak of the power spectral density of the cantilever thermal motion measured with a spectrum analyzer.

For rectangular Si cantilevers operated in UHV, the method proposed by Cleveland and co-workers [37] produces a fair estimation of the cantilever stiffness. In this method, the equivalent static stiffness for the fundamental oscillation mode of the cantilever can be expressed as a function of the resonant frequency and the length and width dimensions of the cantilever. These geometrical dimensions are well defined during the cantilever production process, normally presenting a very low dispersion with respect to the corresponding nominal values, in comparison with the cantilever thickness. In case that it would be impossible to directly measure the cantilever dimensions, good estimations of the length and width values of the cantilevers can be obtained from the quality-control data provided with each cantilever wafer.

The main contribution to the uncertainty in the estimation of the tip–surface interaction force comes, by far, from the determination of the cantilever oscillation amplitude. In an optical interferometer detection scheme, the measured cantilever oscillation amplitude depends on the position of the laser spot along the cantilever longitudinal axis. Values closer to the real oscillation amplitude will be obtained when positioning the laser spot as close as possible to the cantilever free end, over the tip position; otherwise, corrections considering the distance of the laser spot from the cantilever free end must be undertaken. The magnitude of the cantilever oscillation amplitude is normally obtained from the detector output in volt units. A conversion factor to distance units can be calculated using the normalized frequency shift [27]. For an identical tip–surface interaction force and large enough cantilever oscillation amplitudes (see Sect. 3.6), the normalized frequency shift remains constant independently of the oscillation amplitude [13]. Thus, a calibration of the cantilever oscillation amplitude can be performed by tracing the relative tip–sample distance while changing the oscillation amplitude, keeping constant the normalized frequency shift over the same spot on the surface (this requires readjustment of the frequency shift set point for each oscillation amplitude) [24, 38]. A set of several pairs of oscillation amplitude values and corresponding relative tip–sample displacements should follow a linear behavior with slope as the calibration constant. To minimize the influence of piezo creep and assure reproducibility, several cycles increasing and decreasing the cantilever oscillation amplitude can be measured. This calibration should be performed at tip–surface distances corresponding to a significant long-range interaction force, avoiding possible contributions from atomic-scale variations

of the surface. Since the determination of the cantilever oscillation amplitude depends on the position of the laser spot, the calibration should be performed for each experimental session or after repositioning the laser spot on the cantilever.

3.3 Energy Dissipation and Force Spectroscopy

The combination of force spectroscopy and first-principles calculations has contributed in a decisive way to further clarify the enhancement of atomic contrast in the dissipation signal upon increasing the tip–surface short-range interaction force when probing semiconductor surfaces [39].

The dissipation signal is the additional amount of energy that the cantilever requires to keep the oscillation amplitude constant and at resonance under the presence of nonconservative tip–surface interaction forces. This additional energy is put into the cantilever by increasing the voltage amplitude of the harmonic signal applied to the piezoelectric actuator that drives the cantilever oscillation [14]. This voltage is determined by the feedback controller that keeps the oscillation amplitude constant in a FM-AFM detection scheme [5]. The extra excitation applied to compensate reductions in the cantilever oscillation amplitude can be fairly related to the energy dissipated from the cantilever within an oscillation cycle, as it was shown by Cleveand and coworkers [40]. An interesting review on phenomenology and first observations of dissipation signal at atomic scale in FM-AFM together with explanations about the possible origins of this atomic contrast can be found in Chaps. 19 and 20 of the first NC-AFM volume [6].

In those pioneering works, a puzzling experimental observation was that the contrast in the dissipation signal shows a dramatical variability upon modifications of the tip apex [41, 42], indicating a clear dependence of the atomic contrast in the dissipation signal with the nature and structure of the tip termination. It was later suggested that this contrast could even be an artifact due to the electronics regulating the oscillation amplitude [43].

3.3.1 Tip-Apex Characterization Combining Force Spectroscopy and First-Principles Calculations

To contribute to the understanding of the mechanics for the atomic contrast in the dissipation signal, we elaborated force spectroscopy experiments on the Ge(111)-c(2×8) surface. Similar to the Si(111)-(7×7) surface, this germanium reconstruction presents both adatoms and rest atoms terminating the surface [44, 45]. In preliminary experiments on the Ge(111)-c(2×8) surface with AFM, we obtained typically two atomic patterns in topography [46]: one displaying both adatoms and rest atoms (A pattern), usually with a clear dissipation signal registered over the adatom positions; the other showing only the adatoms (B pattern), normally accompanied of a faint atomic contrast

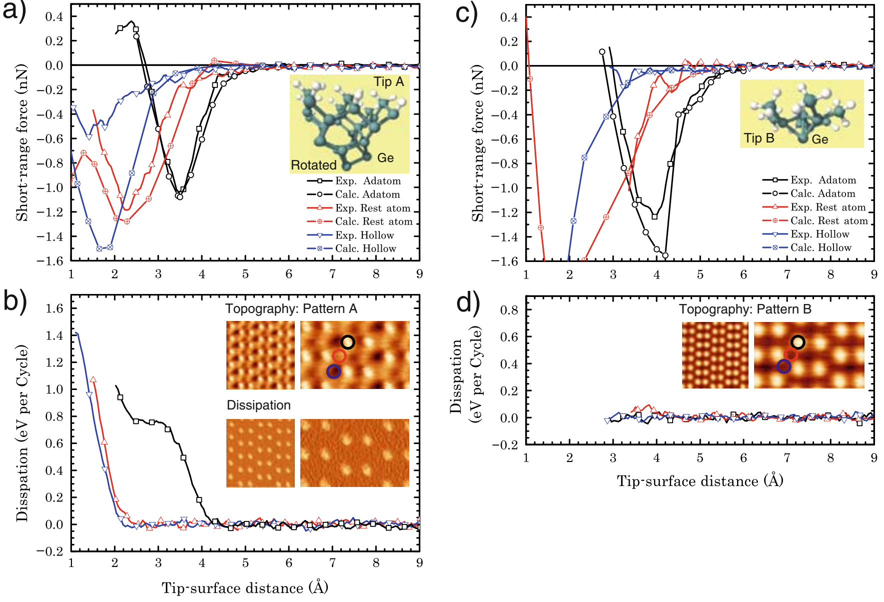

Fig. 3.2. Measured and calculated short-range forces over specific positions of the Ge(111)-c(2×8) surface with two tip terminations producing different atomic patterns. (**a**) and (**b**) Simultaneously measured short-range force and dissipation signal with the tip resolving both adatoms and rest atoms. Simultaneous topographic and dissipation images (A pattern) are displayed as insets. (**c**) and (**d**) Similar data as in (**a**) and (**b**) for a tip resolving only the adatoms of the Ge(111)-c(2×8) surface (B pattern). Acquisition parameters were $f_0 = 183{,}663\,\text{Hz}$, $k = 44 : 3\,\text{N m}^{-1}$, $A_0 = 182\,\text{Å}$, $Q = 259{,}500$ in both cases. Experiments were performed at 80 K tip–surface temperature. The most probable candidates to reproduce the tip termination during the experiments, together with the short-range forces calculated over the adatom, rest atom, and hollow sites using the corresponding tip model are displayed in (**a**) and (**c**), respectively. Figure adapted from [39]

in the dissipation signal, if any. Representative images of these atomic are displayed in Fig. 3.2.

Trying to clarify the origin of these two types of topographic contrast and the presence of atomic contrast in the dissipation signal only in one of them, we measured site-specific force spectroscopic characteristics – simultaneously recording the frequency shift, the cantilever oscillation amplitude, and the dissipation signal – over the adatom, rest atom, and hollow sites of the Ge(111)-c(2×8) surface. We started the measurements with a tip termination producing A pattern imaging. Then, we intentionally modified the tip by producing gentle and controlled contacts with the surface until obtaining a tip termination only resolving the adatoms of the surface and giving no contrast in the dissipation signal. Finally, we repeated the force spectroscopic

measurements with this tip producing B pattern imaging over the same surface sites but at a different location on the surface, keeping exactly the same experimental – resonant frequency, oscillation amplitude, cantilever stiffness, and Q-value – and cantilever dynamic regulation parameters as for the force spectroscopic series acquired with the tip producing A pattern imaging. Only the frequency shift set point was varied from $-15.5\,\mathrm{Hz}$ for imaging with the tip producing A patterns to $-13.4\,\mathrm{Hz}$ for the tip producing B patterns. This corresponds to imaging at very similar maximum total force values (including the long range interaction) of -1.4 and $-1.2\,\mathrm{nN}$, respectively. This procedure rules out possible artifacts in the dissipation signal coming out from the cantilever dynamics regulation electronic.

The short-range force and the dissipation energy measured in these experiments are summarized in Fig. 3.2. Despite the resemblance of the short-range force in both cases (especially over the adatom site), the behavior of the energy dissipated from the cantilever is completely different. A dramatic increment in the dissipation signal is obtained for the tip termination producing A pattern imaging, while complete absence of additional dissipation with respect to the intrinsic energy losses associated with the cantilever oscillation is obtained for the tip providing B patterns, even at the closest tip–sample distances. Interestingly, there is a plateau-like behavior for the dissipation signal over the adatom positions for the tip showing A pattern imaging, in contrast to the monotonic growth for the rest atom and hollow sites.

To elucidate the origin of this behavior in the dissipation signal, we undertook a characterization of the tip–apex termination for each spectroscopic series. This tip characterization is based on an extensive and methodical comparison of the measured short-range forces with the calculated ones using atomically extended and well-tested models to describe the tip–apex structure and composition. For the tip–apex characterization, a set of many possible tip were tested over the adatom and the rest atom positions. Some of these tip models were chosen from the experience gained in previous atomistic simulations [17, 18], others were produced after sharpening a bulk structure by cleaving over different crystalline plane directions, and the rest were the result of heating and quenching process of some of the tip models generated by the cleaving method. Some of these tip terminations are shown in Fig. 3.3.

We found that most of these structures can be grouped into very few families based upon the qualitative force and dissipation characteristics they exhibit, as it also happens in the experiments. A comparison of the calculated force upon approach over the adatom and rest atom positions with the corresponding experimental forces allowed us to perform a first screening. An analysis of the contribution to the interaction force of the different parts of the remaining tip models enabled us to discard some of the structures and to look for an optimum orientation with respect to the surface. Small variations regarding composition and atomic coordination at the very apex enable us a final selection that was based on the best reproduction of the force minima and the attractive and repulsive regions of the experimental curves (Fig. 3.2).

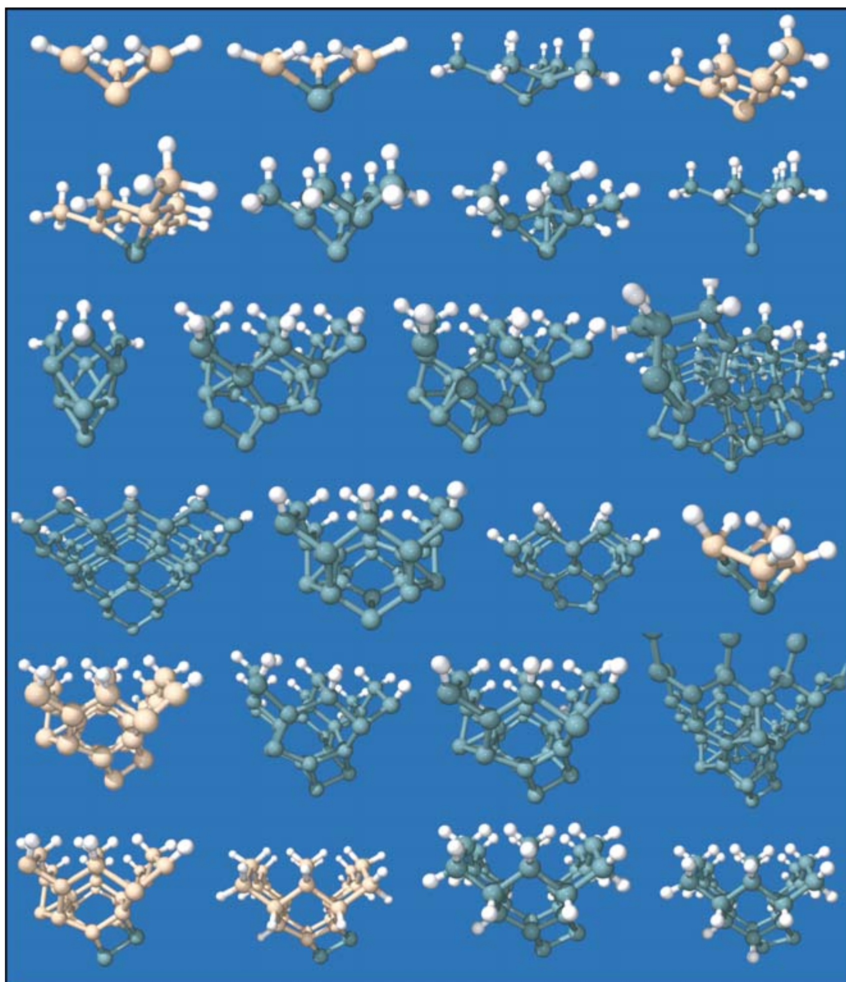

Fig. 3.3. Some of the tip models tested for the characterization of the AFM tip termination during the experiments. The tip characterization is based on an extensive and methodical comparison of the measured and calculated short-range forces. The color code for the tip-model composition is *green* for Ge atoms, *cream* for Si atoms, and *white* hydrogen. Figure adapted from [39]

The tip models satisfying the overall best fit to the experimental curves of both spectroscopic series were selected as candidates to simulate the AFM tip apex during the corresponding experiments.

This tip characterization yielded to an asymmetric Ge dimer terminated tip (tip A in Fig. 3.2) as the most probable candidate to reproduce the tip–apex termination for pattern A imaging. Although the tip A reproduced the force value and the stiffness of the attractive and repulsive regions of the

experimental curve over the adatom, an excessive attractive force over the rest atom was obtained due to the interaction of the tip–apex body with the surrounding Ge adatoms. By rotating the tip A with the dimer line oriented 30° clockwise with respect to the adatom row direction, both the value at the force minimum, and the stiffness of the attractive and repulsive regions were also well reproduced for the rest atom site. In contrast, pattern B imaging was probably produced by a symmetric tip apex terminated in a single atom with a T_4 coordination and a dangling bond pointing perpendicular towards the surface (tip B in Fig. 3.2). The excellent agreement in the comparison of the calculated and the experimental short-range forces for each of these tip models is shown in Fig. 3.2.

3.3.2 Identification of an Energy Dissipation Channel

In previous works, Durig [47], Sasaki, and Tsukada [48] predicted that atomic contrast in the energy dissipated from the cantilever oscillation may be originated by hysteresis in the tip–surface interaction force. Later, Kantorovich and Trevethan [49] elaborated this idea further by applying the soft-mode concept and transition state theory to FM-AFM. In atomistic simulations, these authors showed that energy dissipation of similar values to the ones recorded during experiments can be obtained considering the hysteresis originated by the existence of two or more solutions in the tip–surface interaction force upon approach and retraction of the tip over the surface [49].

In practice, however, it is very difficult to experimentally discern the existence of several solutions in the tip–surface interaction force over one oscillation cycle of the AFM tip. If different force solutions occur, their presence should be blurred when measuring frequency shift curves alone, as the frequency shift is basically a weighted average of the total tip–surface interaction over one oscillation cycle [27, 32]. Thus, experimental forces obtained from continuous frequency shift curves reflect, under normal conditions, only the conservative part of the tip–surface interaction [14]. We have to rely on atomistic simulations to investigate the existence of several force solutions and to corroborate whether there is hysteresis between them that may develop in energy dissipation from the cantilever oscillation.

The characterization of the most probable termination of the tip apex during the experiments described in Sect. 3.3.1 enables to clarify the existence of different force solutions during an approach and retraction cycle of the tip over the surface. Figure 3.4 displays the calculated short-range forces upon the approach and retraction of the tip A and tip B displayed in Fig. 3.2 over an adatom site of the Ge(111)-c(2×8) surface, together with the calculated potential energy as a function of the adatom vertical displacement perpendicular to the surface for different height positions of the corresponding tip model. While in the case of tip B both force curves are very similar, clear hysteresis between two solutions upon approach and retraction appears for the tip A. These two force solutions are associated with a bistability [47, 48] of the

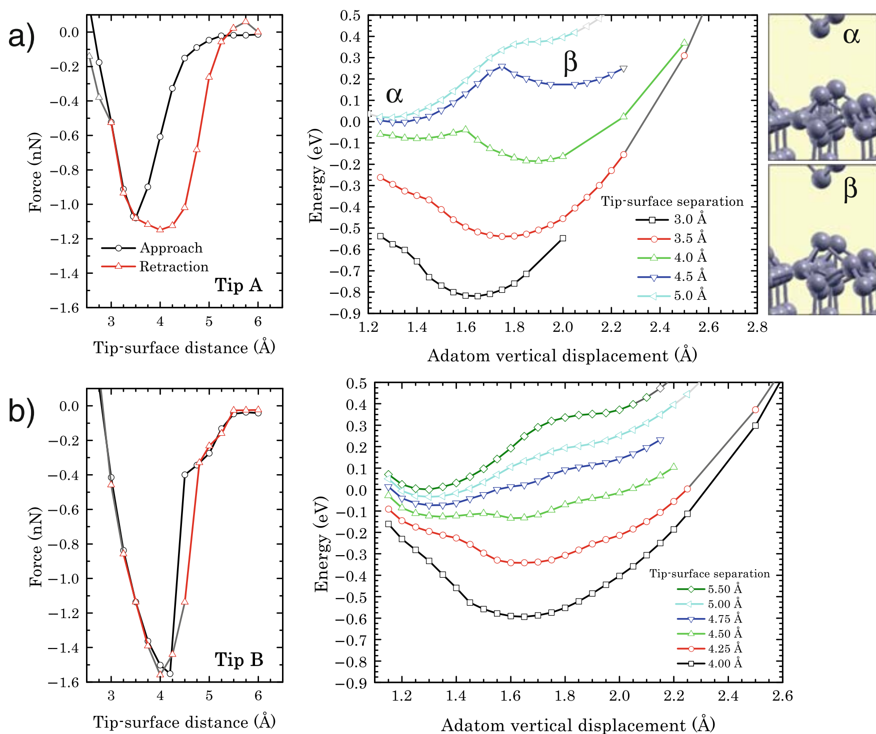

Fig. 3.4. Calculated short-range forces upon a tip approach and retraction cycle over an adatom site of the Ge(111)-c(2×8) surface, and potential energy as a function of the adatom vertical displacement perpendicular to the surface for different tip height positions. (**a**) and (**b**) correspond to calculations performed with the tip A and tip B models displayed in Fig. 3.2, respectively. Figure adapted from [39]

potential energy of the surface adatom due to the tip–apex proximity. The first force solution corresponds to a situation in which the adatom is perfectly sited at its surface position during the tip approach, while the second solution is associated with a situation in which the adatom is slightly pulled out from the surface following the tip retraction (see details of the respective atomic configurations in the images displayed in Fig. 3.4a). The evolution of these two solutions are closely related to the development of two minima at the potential energy curve, labeled as α and β in Fig. 3.4a, upon the surface adatom vertical displacement. The stability of the second force solution during the retraction of the tip model A is originated by the existence of apparent energy barriers between these two minima for a significant tip–surface distance range. The presence of these barriers is favored by structural changes that take place at the apex of tip A during the approach, which lead to a sharpening of the apex structure. Moreover, the accumulation of charge at the lower atom of the dimer at the tip apex reinforces its interaction with the surface adatom

upon retraction. These effects are not present in the single-atom apex of tip B, as it is shown in the potential energy of the surface adatom calculated using the tip B (Fig. 3.4b), leading to almost negligible energy barriers.

Upon these results, the behavior of the measured dissipation signal with the tip–sample distance over a surface adatom with the tip producing A pattern imaging can be explained by taking into account the finite temperature at which the experiments were performed. At zero temperature, a step-like behavior of the dissipation would be expected, as the transition between the two force solutions cannot take place until reaching the tip–surface distance where the barrier goes to zero (around 3.5 Å at the energy plot in Fig. 3.4a). Upon retraction, the system would stay in the second force solution until the barrier for the transition back to the original structure disappears (around 6 Å), following the whole hysteresis cycle shown in the force plot. However, at the tip–sample temperature the experiments were performed (80 K), the system has a probability to overcome these barriers and to jump by thermally activated processes between the two energy minima. This originates transitions between the two force solutions at larger tip–surface distances during the approach and at shorter tip–surface distances during the retraction, completing in this case only a fraction of the whole hysteresis cycle in the force. This situation explains the onset of dissipation at 4.4 Å and the steady increase of the dissipation signal for distances below 3.5 Å in Fig. 3.2b. At tip–surface distances where the barrier for the transition during approach vanishes (below 3.5 Å), the system completes the relevant part of the whole hysteresis cycle by following the first force solution during the tip approach towards the surface and the second solution upon the tip retraction. Under these conditions, the energy dissipation is to be almost steady, reaching the plateau regime. Notice that the energy associated with the hysteresis between the two force solution for the tip A is ∼0.53 eV; a value close to the dissipation signal at which the plateau in the dissipation curve recorded over the adatom is observed (∼0.75 eV, see Fig. 3.2b). Further raising of the dissipation signal after the plateau is originated by the onset of a second dissipation channel involving significant distortions of the tip apex and the adatom configuration, as well as bonding interactions beyond two atoms. This second dissipation channel is closely related to processes, leading to vertical atomic manipulation [50,51] (see Sect. 3.3.4 and Chap. 8), and to tip apex or surface permanent modifications.

The behavior of the dissipation signal with the tip–sample distance for the tip termination producing A pattern imaging at the rest atom and hollow sites in Fig. 3.2b might be originated by a concomitant dissipative interaction between the nearby tip–apex atoms and the neighboring surface adatoms, similar to the adatom case.

Upon these calculations, the energy dissipated from the cantilever oscillation when probing a Ge adatom – located in a T_4 bonding configuration – with a tip producing A pattern imaging is mainly related to the breaking and remaking of the bond with the beneath surface atom, as it is highlighted by

the different bonding configurations for the Ge adatom in the atomic models shown in Fig. 3.4a. The energy dissipation observed at the plateau in Fig. 3.2b might be therefore considered as an estimation of the adhesion associated with this single atomic bond of the Ge adatom with the surface atom underneath.

3.3.3 Surface Adhesion Maps at Atomic Scale

The results described in Sect. 3.3.2 suggest that energy dissipation imaging and spectroscopy measured at atomic scale with FM-AFM may provide information about the adhesion response of surface atoms to a single atomic contact with the tip apex. This information may then be related to the specific nature of the different atomic species forming an heterogeneous surface – leading to an additional channel for atomic recognition – or to variations of the local atomic structure. In this context, the constant height scan and dissipation images of the Si(111)-(7 × 7) surface shown in Fig. 3.5 are of most interest. While in the constant height scan image, the contrast of the Si atoms shows an homogeneous appearance at the respective faulted and unfaulted half unit cells [16, 52], in the dissipation image, the contrast on the corner adatoms considerably differs from that of the center adatoms. Furthermore, while the center adatoms of both half-unit cells present similar contrast in the dissipation signal, the corner adatoms of the faulted-like half-unit cell display less contrast than the corner adatoms of the unfaulted-like half-unit cell. Taking into account the mechanism for the energy dissipation channel described in Sect. 3.3.2, this dissipation image could be considered a map of the adhesion response of the surface adatoms to a single atomic contact with the tip apex, which clearly reveals subtle local structural differences between the adatoms that are imperceptible to the frequency shift. Upon this assumption, the corner adatoms of the faulted-like half-unit cell should be more strongly bonded to the surface than the ones of the unfaulted-like half-unit cell. In addition, a higher vertical mobility of the center adatoms – nearly equal for both half-unit

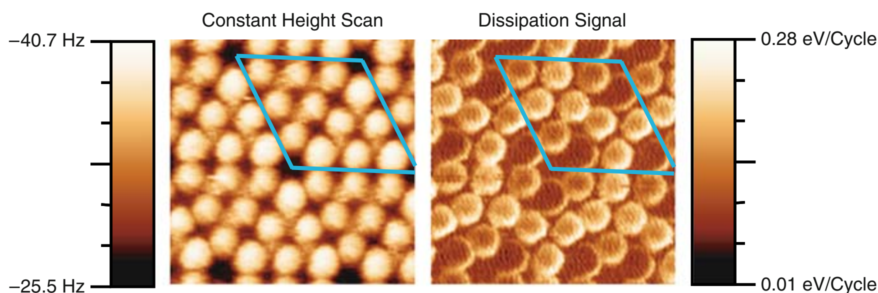

Fig. 3.5. Constant height scan (*left*) and simultaneously measured energy dissipation images of the Si(111)-(7 × 7) surface acquired at 10 K tip–surface temperature. Image size is (5 × 5) nm^2. Acquisition parameters were $f_0 = 173,833.1$ Hz, $K = 37.5\,\text{N m}^{-1}$, $A = 133$ Å, $Q = 91,700$. Figure adapted from [39]

cells – due to a softer interaction with the underlying atoms is expected, in good agreement with previous experimental observations [50,53]. There is also an increment of the dissipation signal in the right-lower part of each adatom independently of its location. These asymmetric structures can be ascribed to the tip apex (because they are common to all the adatoms), and they denote an increment of the adhesion response due to a preferred directionality in the tip–apex configuration, as it has been pointed out in [54, 55].

With a proper tip–apex characterization, atomically resolved dissipation imaging in FM-AFM may develop in quantitative surface adhesion maps at atomic scale.

3.3.4 Signatures of Energy Dissipation in Frequency Shift and Force Curves

In FM-AFM, the frequency shift is proportional to a weighted average of the tip–surface interaction force over one oscillation cycle [14, 27, 32] (see (3.1) and Fig. 3.1). If several force solutions with apparent energy barriers for transitions between them are explored at the closets tip–surface distances, then the presence of these force solutions is going to be smeared off in the frequency shift signal. Thus, frequency shift curves (and the tip–surface interaction forces obtained from them) should not contain information about the nonconservative processes that lead to energy dissipation from the cantilever orcillation [39,48,49]; they are only to reflect the conservative part of the tip–surface interaction [14, 27, 32]. However, in some cases, it is possible to find signatures of nonconservative processes at the tip–surface interface in both frequency shift and force curves, which are subtler than mere discontinuities associated with atomic instabilities either at the tip [33] or at the surface. One example is the spectroscopic curves obtained during vertical interchange manipulation processes [51].

Figure 3.6 shows the variation of the frequency shift, the short-range interaction force, the cantilever oscillation amplitude, and the energy dissipated from the cantilever oscillation, simultaneously recorder during the approach and retraction of the sample over the AFM tip, corresponding to the deposition of a tin atom (Fig. 3.6a) and a silicon atom (Fig. 3.6b) in two consecutive vertical interchange atom manipulation processes, respectively.

A characteristic feature of the frequency shift curves in vertical interchange atom manipulation experiments is the appearance of a shoulder at close tip–surface distances. This shoulder develops into a double well structure in the corresponding short-range interaction force, with similar maximum attractive force values and that seem to concur with a significant increase in the dissipation signal (see Fig. 3.6b and Fig. S2 in [51]). These structures are originated by thermally activated jumps between different force solutions – associated with several energy branches available for the system – as the tip explore distances close to the repulsive regime of the tip–surface short-range interaction,

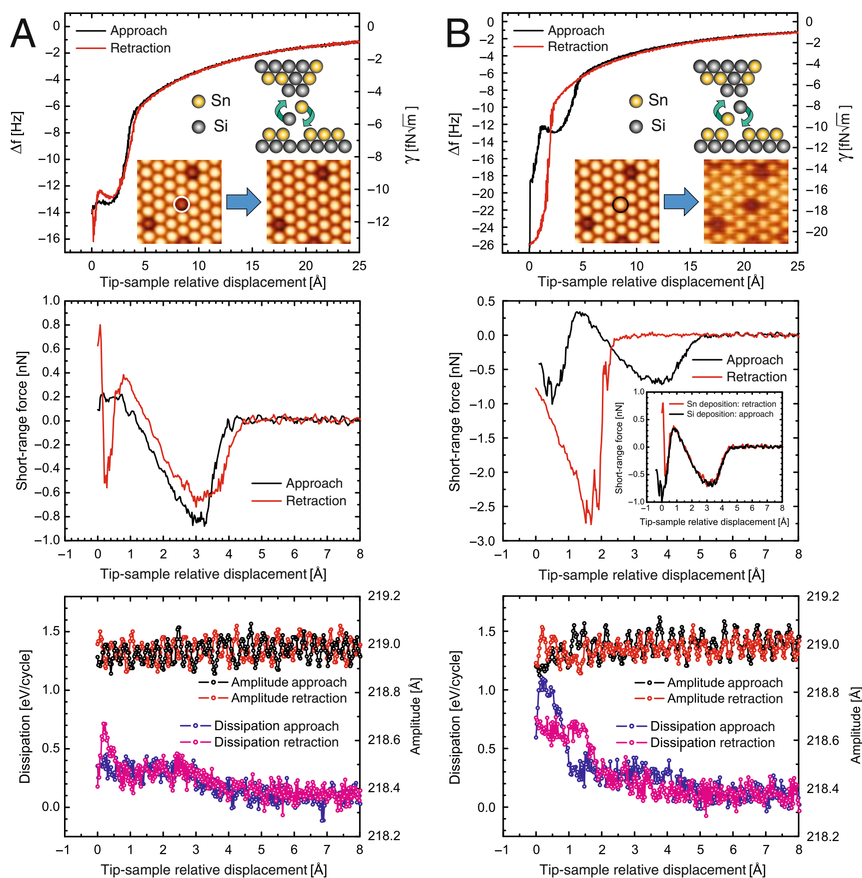

Fig. 3.6. Frequency shift, short-range force, cantilever oscillation amplitude, and energy dissipation per oscillation cycle characteristics simultaneously acquired during the deposition of tin atom (**a**) and a silicon atom (**b**) coming from the AFM tip in two consecutive vertical interchange atom manipulation processes on a Sn/Si(111)-($\sqrt{3} \times \sqrt{3}$)R30° surface. Acquisition parameters were $f_0 = 193{,}738.0$ Hz, $k = 48.8\,\mathrm{N\,m^{-1}}$, $A = 219$ Å, $Q = 13{,}000$. The experiments were performed at room temperature. Figure adapted from [51]

where the atomic rearrangements in the contact area leading to atom manipulation take place [51]. In particular, a double minima in the experimental force curve is an indication of the system evolving between two different bonding configurations during the approach and retraction cycle (see Chap. 11 and the Supplementary Online Material of [51]).

Similar behavior of the tip–surface interaction force has been also observed in force spectroscopy experiments on insulating surfaces like NaCl(100) [56] or MgO(100) (see Fig. 3.7), where a double minima in the force curve appears only over a specific site at the surface. As in the case of the spectroscopic

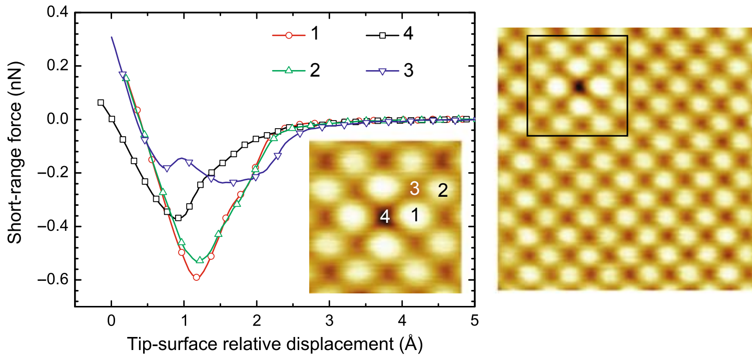

Fig. 3.7. Site-specific force spectroscopy over atomic positions in the vicinity of an atomic defect at the (100) surface of an MgO single crystal. At the sadle-point over the ionic species not resolved in the topographic images (*position 3*), a double-well structure in the short-range force is clearly observed. These minima can be ascribed to transitions between different force solutions accessible for the tip–surface system. Acquisition parameters were $f_0 = 175{,}048.0\,\mathrm{Hz}$, $k = 38.3\,\mathrm{N\,m^{-1}}$, $A = 24\,\text{Å}$, $Q = 186{,}857$. Experiments were performed at 80 K tip–sample temperature. Image sizes are $(2.5 \times 2.5)\,\mathrm{nm}^2$ and $(1.0 \times 1.0)\,\mathrm{nm}^2$

curves in vertical interchange atom manipulation experiments, the presence of these double minima may be ascribed to transitions between different force solutions accessible for the tip–surface system. The energy barriers for the transitions between these different force solutions as a function of the tip–surface distance dictate where the system jumps during either approach or retraction in an stochastic process driven by the available thermal energy and, thus, determine the details of both frequency shift and force curves.

3.4 Force Spectroscopy and Atomic Relaxations

The combination of interatomic force measurements on heterogeneous semiconductor surfaces and first-principle calculations has also enabled to clarify the relation between striking observations of the topographic contrast at close tip–surface distances, the real surface structure, and role played by atomic relaxations of the closest tip and surface atoms [36].

Figure 3.8 summarizes the behavior of the topographic contrast when imaging silicon defects (protrusions with diminished contrast) at the perfect single-atomic later of tin atoms (bright protrusions) that form the Sn/Si(111)-$(\sqrt{3} \times \sqrt{3})R30°$ surface [57, 58]. For a low density of defects, these Si atoms are usually equally surrounded by six Sn atoms, showing an identical height difference with respect to the Sn atoms. We have found, however, a reduction of the relative topographic height between Sn and Si upon increasing the tip–surface interaction force. This effect is shown in Fig. 3.8d, where the

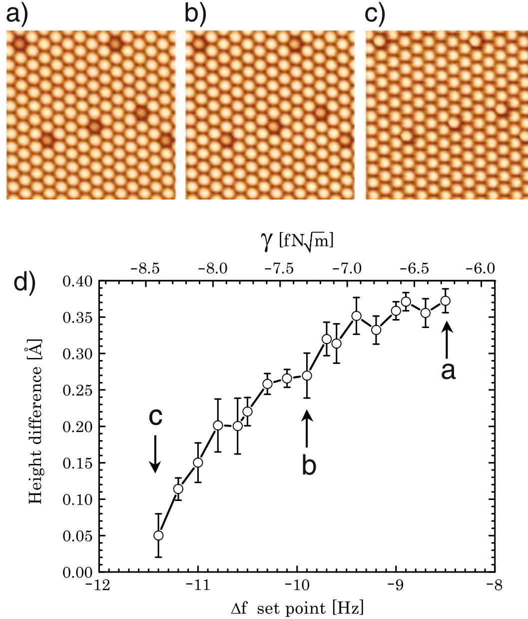

Fig. 3.8. (**a**)–(**c**) Images showing the reduction of the topographic height difference between substitutional silicon defects and the tin atoms of the Sn/Si(111)-($\sqrt{3} \times \sqrt{3})R30^\circ$ surface when decreasing the tip–sample distance. Image dimensions are $(8.5 \times 8.5)\,\mathrm{nm}^2$. (**d**) Dependence of the Sn–Si topographic height difference with the frequency shift image set point. Acquisition parameters were $f_0 = 162{,}285.8\,\mathrm{Hz}$, $k = 30.5\,\mathrm{N\,m}^{-1}$, and $A = 200\,\mathrm{Å}$. Figure adapted from [36]

topographic height difference between Sn and Si is quantified from a series of images measured – over the same surface area and with the same tip apex termination – consecutively increasing the absolute value of the frequency shift imaging set point. As is evidenced by the images depicted in Fig. 3.8a–c, the Sn–Si height difference decreases almost up to disappearance at the closest tip–surface distances.

The atomically resolved topography images displayed in Fig. 3.8 are consequence of the forces associated with the bonding interaction between the outermost atom of the tip apex and the surface atoms [17, 18]. It has been demonstrated that atoms on heterogeneous semiconductor surfaces occupying nonequivalent positions provide a different force response to the interaction with the AFM tip [59, 60]. This is not the case in the surface under consideration here, as both Sn and Si are occupying equivalent T_4 adsorption positions over the Si(111) surface, each atom having four valence electrons in a sp^3-like-hybridization and one dangling bond pointing outwards from the surface plane. Thus, the reduction of the Sn–Si topographic height difference when decreasing the tip–surface distance suggests several possible scenarios:

one, that there is a different chemical interaction between the Sn and the Si atoms, respectively, with the tip apex; other, that the interaction with the AFM tip produces structural vertical distortions of the atoms that manifest in a reduction of the topographic height difference; finally, there may occur a combination of these two cases depending on the strength of the interaction force. Information to further clarify this matter can be obtained by the analysis of site-specific force spectroscopic measurements.

Figure 3.9a shows frequency shift curves measured over the Sn and the Si atoms pointed out in the inset image. These curves were measured using the atom tracking technique to assure a precision in positioning the AFM tip over the topmost part of the surface atoms better than ± 0.1 Å [24–26]. Measuring site-specific force spectroscopic characteristics with the atom tracking technique requires locking onto the top-most par of the surface atom using the topographic signal (see Chap. 2 for details). In the case of heterogeneous surfaces with atoms showing variability in the topographic contrast, this procedure causes variations in the absolute tip–surface distance at which the acquisition of the frequency shift curve starts for the different atoms. For instance, when probing an Si adatom using a set point close to the onset of significant short-range interaction force, the tip is going to be closer to the sample than in the case of an Sn atom. This effect manifests in a different trend in the long-range interaction region of the frequency shift curves, which in principle should be common to all the curves measured with the same AFM tip in a surface area where local variations of the long-range interaction are not expected. This different trend in the long-range interaction is apparent in the curves shown in Fig. 3.9a. These curves meet at a frequency shift value of -5.4 Hz (the set point for the topographic feedback during both imaging and atom-tracking operation), point that corresponds to the origin of the relative tip–sample displacement (see the upper scale). A fair comparison of these curves, as well as the force curves obtained later on, requires compensation of this topographic effect associated with the acquisition protocol. Common values in the tip–sample displacement with respect to the surface plane are obtained by shifting the curve measured over the Si atom by a distance that matches the measured Sn–Si height difference at the given frequency shift topographic set point at which the curves were acquired. From the image recorded after the spectroscopic acquisition (inset in Fig. 3.9a), this distance corresponds to 0.54 Å (see the topographic profile displayed in Fig. 3.9b). The frequency shift curves after the topographic effect compensation are shown in Fig. 3.9b; now both curves share the same behavior over the long-range interaction region up to reaching the tip–surface distance where the contribution of the short-range interaction over the Sn atom becomes dominant.

The new crossing point of the frequency shift curves displayed in Fig. 3.9b provides an explanation for the reduction of the topographic height difference between Sn and Si upon decreasing the tip–surface distance (Fig. 3.8). According to the curves in Fig. 3.9b, the difference in topography at a given imaging set point should gradually decrease when increasing the absolute value of the

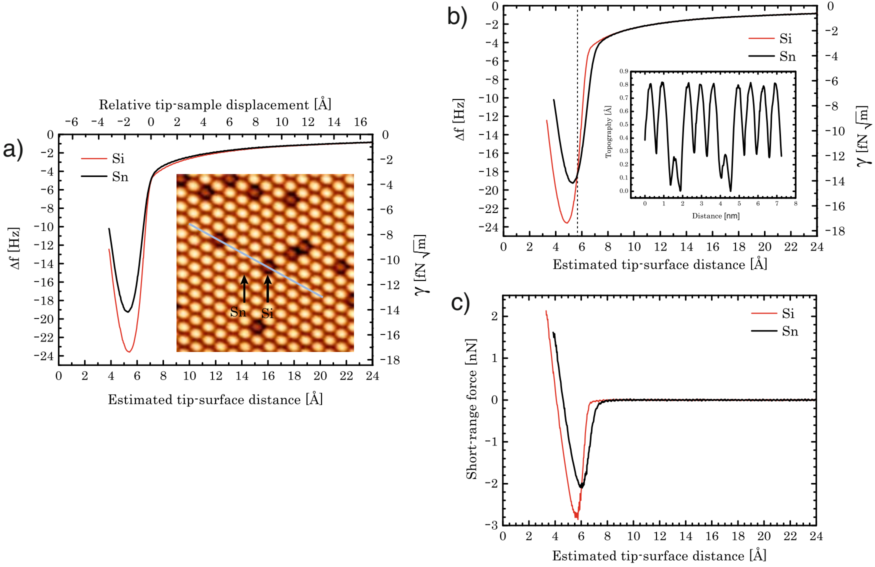

Fig. 3.9. (**a**) and (**b**) Force spectroscopic measurements over the Si and the Sn atoms pointed out the inset image. In (**b**), the frequency shift curve for the Si atom has been shifted by the height difference between Sn and Si (measured from the image in (**a**) and shown in the inset profile) to compensate the topographic effects associated with acquisition using the atom tracking technique. The *dotted line* highlight the position of the crossing point between both curves. Acquisition parameters were $f_0 = 162285.8$ Hz, $k = 30.5$ N/m, and $A = 259$ Å. The frequency shift set point for imaging and atom-tracking operation was -5.4 Hz. Image size is (8.5×8.5) nm^2. (**c**) Short-range forces corresponding to the frequency shift curves shown in (**b**). The tip–surface distance in estimated by assuming the surface position at the divergence for the fitting to the long-range contribution. Figure adapted from [36]

frequency shift up to reaching the crossing point, at which both atomic species would present the same height. This behavior is due to a different strength in the bonding interaction of Sn and Si, respectively, with the outermost atom of the tip apex, as it is evidenced by the corresponding short-range force characteristics displayed in Fig. 3.9c: the bonding force over the Sn atom is sensed at farther tip–surface distances, and, additionally, the value of the maximum attractive force is larger for the Si atom.

Contributions from atomic relaxations due to the interaction with the tip apex cannot be neglected as possible origin of the topographic height differences between Sn and Si. To investigate their influence, we have relied on atomistic simulations and the ability to characterize the most probable tip–apex termination during the experiments by the combination of force spectroscopic measurements and first-principles calculations (see Sect. 3.3.1).

Figure 3.10a shows the comparison of the short-range forces obtained from first-principles calculations upon approaching the tip model depicted in

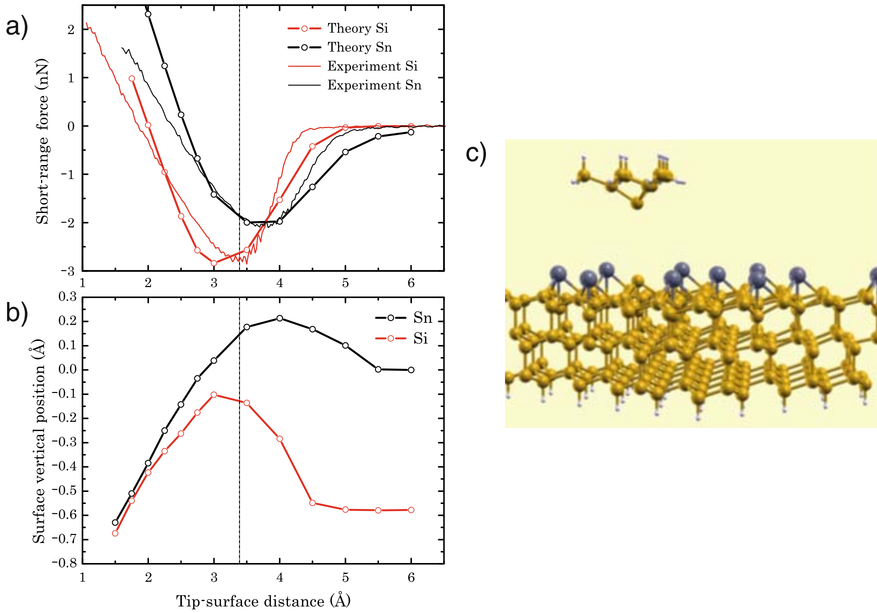

Fig. 3.10. (**a**) Comparison of the measured short-range forces displayed in Fig. 3.9c with the calculated interaction force of the tip model depicted in (**c**) with a Sn and a Si atom of the Sn/Si(111)-($\sqrt{3} \times \sqrt{3}$)$R30°$ surface, respectively. (**b**) Induced relaxations of the vertical position of the surface atoms due to the interaction with the tip model. The *dotted lines* denote the position of the crossing point between the frequency shift curves in Fig. 3.9b. For a proper comparison with the theoretical curves, the experimental force curves and the dotted line were shifted as a unit by 2.25 Å with respect to Fig. 3.9c, to align the minima of the force curves obtained over the Sn atom. Figure adapted from [36]

Fig. 3.10c – representing a quite stiff tip-apex termination – on a Sn and a Si atom of the Sn/Si(111)-($\sqrt{3} \times \sqrt{3}$)$R30°$ surface with the corresponding experimental curves (shown in Fig. 3.9c) over the closest tip–surface distance rage. Although the agreement between the force values at the minima is excellent, the stiffness of the attractive and repulsive interaction regions (i.e., the slope of the force curve in each of these two regimes) slightly differs from those of the experimental curves. This difference may be originated by a higher softness of the real tip apex during the experiments, which would allow atomic relaxations beyond the atomic positions considered in the tip model to accommodate the stress caused by the interaction with the surface, either in the attractive or the repulsive regime. Simulations using more realistic tip models [39, 55] have provided short-range force curves in a notable good agreement with the experimental ones, in both the maximum attractive force and the stiffness of the attractive and repulsive regimes [39] (see Sect. 3.3.1). The excellent agreement between the maximum attractive force values of the experimental and calculated short-renge force curves in Fig. 3.10a suggests, however, a tip-apex

termination during the experiment in the form of a Si atom with a single dangling bond pointing perpendicular towards the surface plane.

The analysis of the vertical displacements of the surface atoms upon proximity of the tip model (Fig. 3.10b) indicates that the attractive interaction with the tip originates local distortions that lift the Si atom upwards slightly more than for the Sn atom. At very low interaction forces, the height difference between Sn and Si remains close to the value for the isolated surface (∼0.5 Å). Upon increasing the attractive interaction force, both surface adatoms experience a vertical relaxation towards the tip, which is more prominent in the case of the Si atom. The onset of the covalent bonding with the tip outermost atom provides extra charge to the surface Si atom (that initially has a charge deficiency due to a charge transfer to the neighboring Sn atoms [61]), favoring a larger vertical displacement than that of the Sn atom. At a tip–surface distance close to the force minimum, there is a strong relaxation of both the tip outermost atom and the surface atom in order to accommodate an atomic separation between them similar to the sum of the corresponding covalent radii. This situation has important consequences for the single-atom chemical identification capability of AFM, as it is discussed in Sect. 3.5. At tip–surface separations smaller than the distance for the maximum attractive force, the surface atoms relax back towards the surface due to Pauli repulsion of the electron clouds of the interacting tip and surface atoms.

These results suggest that when imaging heterogeneous semiconductor surfaces, FM-AFM can provide a fairly direct access to the true structure of the surface. In principle, topographic measurements does not correspond to the real height difference between surface atoms, as the topography measured with FM-AFM is a complicated convolution of the total tip–surface interaction (which shows variability upon different tip-apex terminations, see Sect. 3.5) and the structure of the surface (that can also be affected by the interaction with the tip). However, the results described here show that when imaging at the onset of the short-range interaction (exploring weak forces that barely disturb the surface structure), the registered corrugation seems to closely reproduce the real atomic height differences expected for the free surface. At smaller tip–surface separations, the tip–surface interaction gradually produces significant displacements of both tip and surface atoms during every oscillation cycle, and differences in the strength of the short-range interaction intrinsic to each of the atomic species composing the surface start to dominate over the distance dependence; under these conditions, the measured topographic contrast cannot be related anymore to the geometry of the free surface.

3.5 Single Atom Chemical Identification

When exploring semiconductor surfaces with FM-AFM, atomic contrast is obtained by detecting the forces associated with the onset of a bond formation between the outermost atom of the AFM tip and the atoms at the surface

[17, 18]. In the case of heterogeneous surfaces, these short-range forces will show small variations for the different atomic species composing the surface. An example of this behavior can be seen in Figs. 3.9 and 3.10. Thus, these inter-atomic forces should contain information about the chemical nature of the different surface atoms, and, in principle, the precise quantification of the tip–surface short-range force over each atom at the surface should lead to the possibility of chemically identifying them.

The realization of this concept is, however, quite complex as the short-range forces obtained with FM-AFM ultimately depend on the tip-apex termination. This variability of the measured forces with the AFM tip is shown in Fig. 3.11b–f, where several sets of short-range force curves obtained over Sn and Si atoms of the Sn/Si(111)-($\sqrt{3} \times \sqrt{3}$)R30° surface are displayed. These sets of force curves were obtained over Sn and Si atoms in an equivalent local surface configuration similar to the one shown in Fig. 3.11a, using identical acquisition and analysis protocols (see [62] for details) but over multiple measurement sessions involving different tip–apex terminations. Some of these sets were even measured with the same cantilever and acquisition parameters – resonant frequency, oscillation amplitude, cantilever stiffness, and Q-value – but after intentionally modifying the tip apex by producing gentle tip–surface contacts. The comparison of all these sets of force curves (Fig. 3.11g) reveals a strong tip dependence of both the registered maximum attractive force values and the distance dependence of the forces over the attractive and repulsive regimens.

In spite of the variability of the measured forces with the AFM tip, we have found a parameter that remains nearly constant, independently of the tip–apex termination [62]. This parameter is the relative interaction ratio of the maximum attractive short-range force within a set of force curves measured with the same tip. A graphical visualization of this parameter can be obtained by normalizing the two curves within each set by the absolute value of the maximum attractive force registered over the Si atom ($|F_{\mathrm{Si(Set)}}|$). Doing so, the curves corresponding to the Si atom will present their minimum value at the unit, and the curves measured over the Sn atoms will display their minimum value at the relative interaction ratio. The result of applying this normalization for all the sets of force curves shown in Fig. 3.11 is displayed in Fig. 3.11h, revealing an average value of the relative interaction ratio for Sn calibrated against Si of 0.77 ± 0.02.

These findings have been reproduced on other surfaces with similar structure but different chemical composition, like the Pb/Si(111)-($\sqrt{3} \times \sqrt{3}$)R30° and the In/Si(111)-($\sqrt{3} \times \sqrt{3}$)R30° surfaces. Sets of short-range force curves were also obtained for these surfaces over structurally equivalent atoms to the ones pointed out in the insets of Figs. 3.12a and b, using identical acquisition and analysis protocols as for the Sn and Si case. Again, different behavior of the maximum attractive force value and the distance dependence of the force over the attractive and repulsive regions is obtained for different

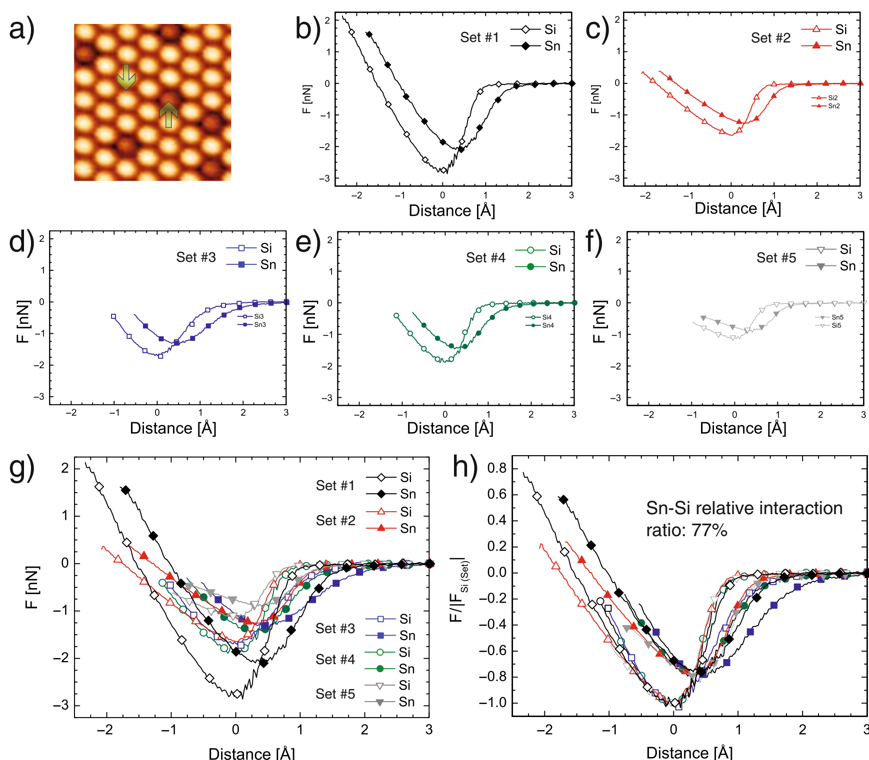

Fig. 3.11. (**a**) Topographic image of the Sn/Si(111)-($\sqrt{3} \times \sqrt{3}$)R30° surface. (**b**)–(**f**) Sets of short-range force curves obtained over structurally equivalent Sn (bright protrusions) and Si atoms as the ones pointed out in (**a**), using identical acquisition and analysis protocols but different tip terminations. (**g**) Comparison of all the sets of force curves. (**h**) Curves shown in (**b**)–(**f**) normalized to the corresponding absolute value of the maximum attractive short-range force registered over the Si atom ($|F_{Si(Set)}|$) within each set. The acquisition parameters are available in the supplementary information accompanying the publication from which the figures are adapted [62]

tip–apex terminations. There is only one apparent common feature to all the sets of force curves shown in Figs. 3.11 and 3.12: the curve obtained over the Si atom provides the stronger attractive interaction force. When performing the same normalization as in the Sn and Si case over the sets measured on the Pb/Si(111) and In/Si(111) surfaces, identical behavior is confirmed: the curves measured over the Si atoms meet at the force minima, and the curves obtained over Pb and In atoms coincide again at the corresponding minima, revealing an average relative interaction ratio for Pb calibrated against Si of 0.59 ± 0.03 (Fig. 3.12a), and a relative interaction ratio for In calibrated also against Si of 0.72 ± 0.04 (Fig. 3.12b).

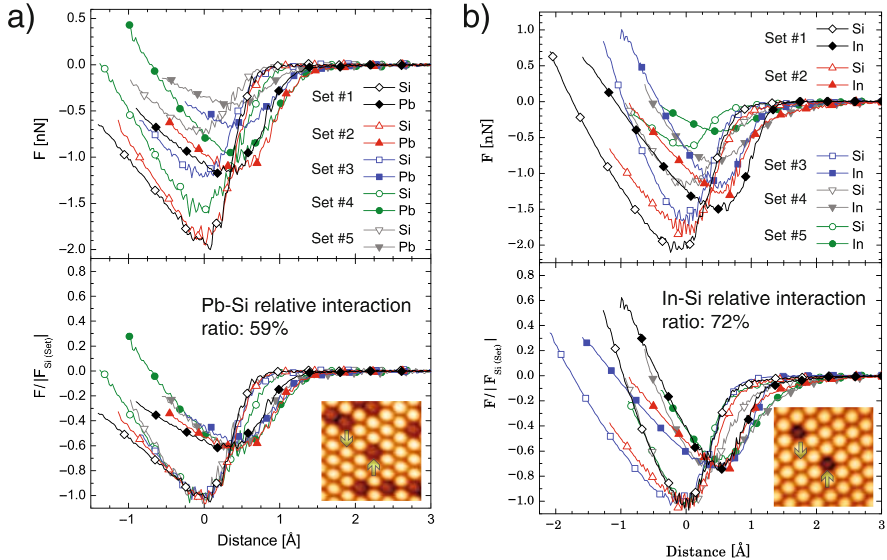

Fig. 3.12. Sets of short-range force curves obtained over Pb and Si atoms of the Pb/Si(111)-($\sqrt{3} \times \sqrt{3}$)R30° surface (**a**), and In and Si atoms of the In/Si(111)-($\sqrt{3} \times \sqrt{3}$)R30° surface (**b**), using identical acquisition and analysis protocols as in the experiments shown in Fig. 3.11. These measurements reproduce the findings described in detail for the Sn/Si(111) system yet in other surfaces with similar structure but different chemical composition. From these experiments, it is obtained an average relative interaction ratio for Pb and In calibrated against Si of 59 and 72%, respectively. The acquisition parameters are available in the supplementary information accompanying the publication from which the figures are adapted [62]

Insights into the behavior of the force curves upon acquisition with different tip–apex terminations, and into the essence of the relative interaction ratio, can be gained from first-principles simulations and modeling [62]. Calculations of the short-range interaction force over a Sn and a Si atom of the Sn/Si(111)-($\sqrt{3} \times \sqrt{3}$)R30° surface using different tip-apex terminations are shown in Fig. 3.13. Sets of force curves calculated with homogenous tip apexes made of Si but with different structure (Tip 1 and Tip 3 in Fig. 3.13) reveal a strong variability of the force values with the tip–surface distance, pointing towards a clear dependence of the measured forces on the structure and elasticity response of the tip apex. Sets of force curves calculated with tip models of identical structure but different chemical termination among the reasonable species involved in the experiments (that is Sn and Si) also produce disparities in the behavior of the short-range interaction. Weaker force values are obtained for Sn terminated tips, as it is evidenced by the comparison of the curves calculated with Tip 2 and Tip 4 with the ones obtained using Tip 1 and Tip 3 in Fig. 3.13, respectively. In all these cases, the strongest interaction is always registered over the Si atom, as it is observed also in the experiments.

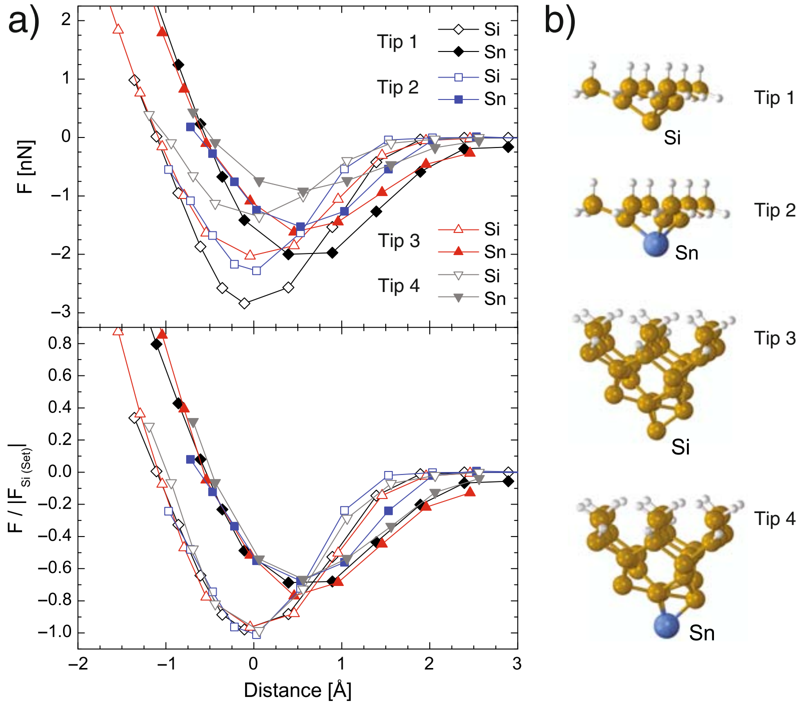

Fig. 3.13. (**a**) Sets of short-range force curves calculated over Sn and Si atoms of the Sn/Si(111)-($\sqrt{3} \times \sqrt{3}$)R30° surface using the tip models shown in (**b**). The force curves are depicted before (*upper graph*) and after (*lower graph*) the normalization of both curves within each set to the corresponding absolute value of the maximum attractive force obtained over the Si atom. Figure adapted from [62]

In spite of these differences, and independently of the tip–apex structure and chemical termination, when applying the same normalization procedure as in Fig. 3.11 to each set of force curves, all the curves calculated over Si and Sn atoms meet at the minima, leading to an average relative interaction ratio for Sn calibrated against Si of 0.71 ± 0.07 (Fig. 3.13); value quite close to the experimental one. These calculations suggest that, for tips providing a short-range interaction of enough strength to obtain atomic resolution, the relative interaction ratio seems to be independent of the chemical termination of the tip apex.

A basic interpretation of the relative interaction ratio can be gained from our current understanding of the imaging mechanism on semiconductor surfaces. As it is shown in Sect. 3.4, when probing the surface close to the onset of the short-range interaction, the surface structure is almost unperturbed [36]. However, close to tip–surface distances that correspond to the maximum attractive short-range force, there are important distortions of the interacting atoms at both tip and surface (see Sect. 3.4) [36]. In this situation, the dom-

inant contribution to the interaction comes from the bonding between the outermost atom of the AFM tip and the atom probed at the surface, which can be considered as they were almost forming a dimer-like structure. This dimer-like interaction could be roughly associated with the bond stretching (or pair-wise) term that is used as the fundamental energetic contribution in many approximate descriptions of the atomic bonding [63]. Under this approximation, the heterogeneous covalent interaction potential between a pair of elements t and α can be estimated as the geometric mean of the homogeneous interaction potential of the corresponding elements, $t-t$ and $\alpha-\alpha$, that is, $E^0_{t-\alpha} \approx \sqrt{E^0_{t-t} \times E^0_{\alpha-\alpha}}$. According to the bond stretching properties, the maximum attractive force $F_{t-\alpha,\max}$ should be proportional to the dissociation energy $E^0_{t-\alpha}$ divided by a characteristic decay length $R^*_{t-\alpha}$ of the interaction, that is, $F_{t-\alpha,\max} \propto E^0_{t-\alpha}/R^*_{t-\alpha}$. Thus, for a given tip–apex of unknown chemical termination, when considering the short-range interaction force of the tip outermost atom t with two separate surface atoms α and β evaluated at the force minima ($F_{t-\alpha,\max}$ and $F_{t-\beta,\max}$, respectively), if the differences between $R^*_{\alpha-t}$, $R^*_{\beta-t}$, $R^*_{\alpha-\alpha}$, $R^*_{\beta-\beta}$ and R^*_{t-t} are small enough, the relative interaction ratio could be approximated by the expression:

$$\frac{F_{t-\alpha,\max}}{F_{t-\beta,\max}} \approx \frac{\sqrt{F_{t-t,\max} \times F_{\alpha-\alpha,\max}}}{\sqrt{F_{t-t,\max} \times F_{\beta-\beta,\max}}} \approx \sqrt{\frac{F_{\alpha-\alpha,\max}}{F_{\beta-\beta,\max}}} \tag{3.3}$$

where $F_{t-t,\max}$, $F_{\alpha-\alpha,\max}$, and $F_{\beta-\beta,\max}$ denote the homogeneous short-range interaction force of the corresponding elements evaluated at the maximum attractive force.

The short-range force curves acquired over a given surface atom are expected to depend on the elastic response of tip and surface [36, 39, 55, 64], the chemical composition and structure of the tip apex [62], and its relative orientation with respect to the surface [65, 66]. However, when taking the relative interaction ratio of the maximum attractive short-range forces for two atomic species probed with the same tip, the common features associated with the structural characteristics of the tip–apex cancel out, and the influence of the chemical nature of the tip–apex outermost atom is minimized. Upon the presence of a certain covalent component in the tip–surface short-range interaction, the relative interaction ration becomes a quantification of the relative strength the surface atoms have to interact with the outermost atom of the tip, as it is pointed out by (3.3). This property can be generalized to multielement systems, as when individually probing different atoms at a surface with a given tip–apex termination, interactions between pairs of atomic species are to be obtained.

The independence of the relative interaction ratio from the tip–apex termination provides the basis for the formulation of a single-atom chemical identification protocol with FM-AFM. The identification procedure requires first the calibration of the relative interaction ratio for the atomic species involved with respect to one of them, typically the one providing the strongest interaction force. The determination of the maximum attractive short-range

force over each surface atom and comparison of their ratio with the tabulated values of the relative interaction ratio will allow them to identify the atomic species composing a multielement system, upon enough precision in both the quantification of the short-range interaction forces and the calibration of the corresponding relative interaction ratios.

We have demonstrated this protocol by merging Sn, Pb, and Si atoms on the same surface under equal proportions. An image of such system is displayed in Fig. 3.14a. The analysis of the topographic height difference between the atoms in Fig. 3.14a reveals nothing more than what is evident by simple inspection: there are only two visible groups of atoms, one presenting a bright contrast and other showing a diminished contrast. From the experience gained in the study of the Sn/Si(111), Pb/Si(111), and In/Si(111) surfaces, one could predict that the atoms with lessen contrast would correspond to Si (see images in Figs. 3.11 and 3.12); however, a priori, there is no clue to discern what protrusions correspond to Pb atoms and which ones to Sn. After systematically performing force spectroscopic measurements over each atom of the image, the quantification of the maximum attractive force values clearly reveals three groups of forces (Fig. 3.14d). When evaluating the ratios between the average force values representing these groups of forces, they match with the relative interaction ratio for Sn and Pb calibrated against Si, obtained from previous experiments (Figs. 3.11 and 3.12). This comparison allows us to correlate each group of forces with one of the atomic species (Fig. 3.14d), and, therefore, identity each surface atom as it is shown in Fig. 3.14c, where blue, green, and red colored atoms correspond to Sn, Pb, and Si, respectively.

Our initial hypothesis that protrusions showing lesser contrast correspond to Si atoms was right. Nevertheless, not always atoms with diminished contrast are Si. Figures 3.14e–h present a similar analysis performed over another area of this surface alloy composed by a mixture of Sn, Pb, and Si atoms. In this case, Pb atoms almost completely surrounded by Si (atoms marked in Fig. 3.14e by a darker shade of green) present identical topographic contrast to most of the Si atoms in the image. These variations in the topographic height of Pb atoms with the number of first-neighboring Si atoms have been attributed to a subtle coupling between charge-transfer and atomic-relaxations [61], which also influence the chemical response of the Pb atom with respect to the interaction with the AFM tip. The identification method described here was, however, robust enough to identify these Pb atoms even upon variations of their chemical properties.

We believe that the capability of AFM for the identification of individual atoms holds substantial promise for widening the applicability of this techniques to studies on heterogeneous surfaces, in which important functional properties are controlled by the chemical nature and short-range ordering of individual atoms, defects, adsorbates, or dopants. In particular, the combination of this identification method with the ability of the AFM for the atom manipulation [51,67,68] may bring future atom-based technological enterprises closer to reality. Furthermore, correlations between chemical specificity, short-

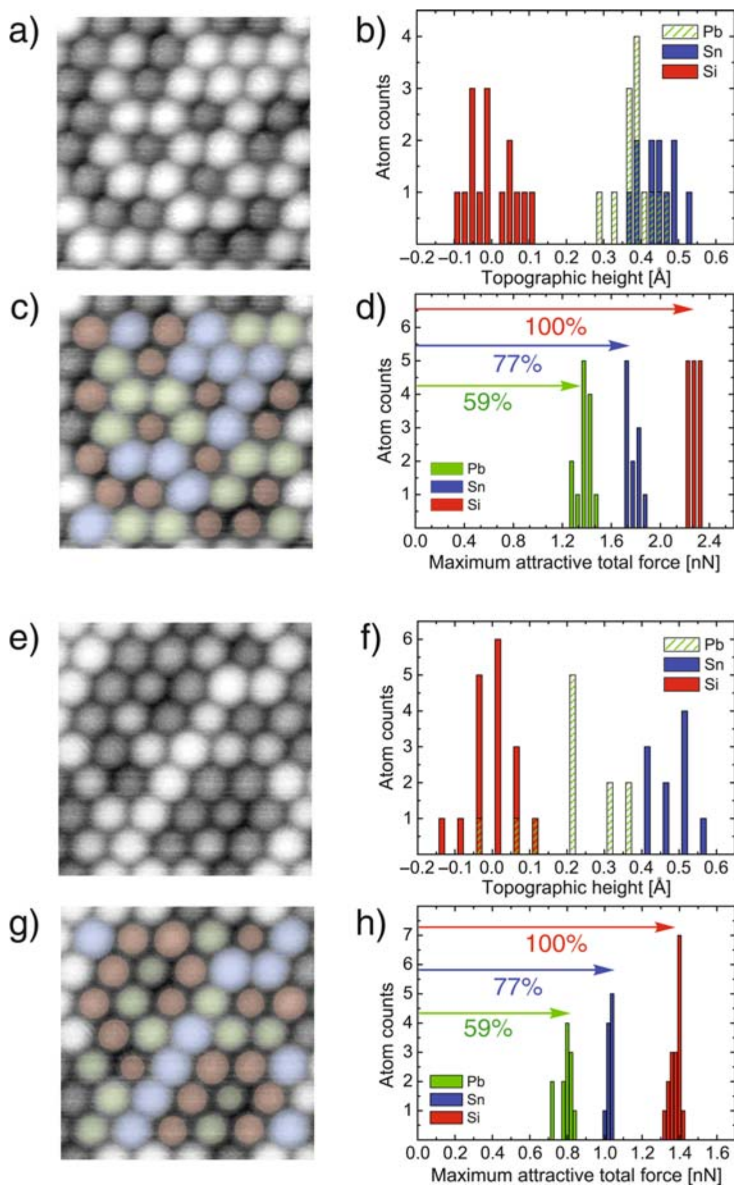

Fig. 3.14. Series of figures demonstrating chemical specificity of AFM. See text for details. Acquisition parameters can be found in the supplementary information of [62], from which the figure has been adapted

range interaction forces, Kelvin probe force microscopy, and energy dissipation measurements at atomic scale on heterogeneous surfaces may provide new insights into AFM phenomenology, and even help to develop a new and more refined identification protocol, as all these magnitudes are sensitive to the chemical nature of the surface atoms.

3.6 Force Spectroscopy with Higher Flexural Modes

Currently, there is a clear trend to operate FM-AFM using small cantilever oscillation amplitudes. It has been predicted improvements in both force sensibility and spatial resolution by reducing the cantilever oscillation amplitude to values close to the decay length of the short-range interactions responsible for atomic contrast in FM-AFM [69, 70]. Nevertheless, there is a limit on the reduction of the oscillation amplitude, which is imposed by the need of keeping the cantilever oscillation stable at close proximity to the surface [71].

Stable cantilever oscillation requires a restoring force at the closest tip–surface distance greater than the tip–surface interaction, to avoid snap to contact of the tip over the surface [8, 71]:

$$k_{\mathrm{s}} A_0 > \max(-F_{\mathrm{int}}),$$

where k_{s}, A_0, and F_{int} denote the cantilever static stiffness, the cantilever oscillation amplitude, and the tip–surface interaction force, respectively.

In addition, the presence of nonconservative interactions at small tip–surface separations generates dissipation of energy from the cantilever oscillation (see Sect. 3.3). This energy dissipation can create fluctuations of the oscillation amplitude that may reflect in an increment of the noise in the frequency shift signal due to slight variations of the tip–surface distance [71], and eventually they might develop into an unstable cantilever oscillation. Thus, proper control of the oscillation amplitude requires that the energy dissipated from the cantilever oscillation per cycle (ΔE_{TS}) should be smaller than the intrinsic energy lost by the cantilever oscillation (E_0) within the time lag in which the amplitude feedback responds to a variation of the oscillation amplitude [71]:

$$E_{\mathrm{TS}} < E_0 = \frac{\pi k_{\mathrm{s}} A_0^2}{Q}.$$

Fulfillment of these stability criteria and pursuance of high sensibility in force detection with small oscillation amplitudes demand the use of cantilevers with (i) high resonant frequencies; (ii) large static stiffness; (iii) high Q values (yet not excessively large so that it could make difficult controlling the oscillation amplitude).

Nowadays, there are several implementations that meet these requirements. One is the use of small cantilevers and special optical interferometers to focus the laser beam on them [72, 73]. A more popular approach is the

implementation of the qPlus sensor [74, 75]. But for an AFM based on standard cantilevers and optical interferometric detection, a straight forward solution may be to operate FM-AFM using the cantilever higher flexural modes [76,77]. These modes are characterized by a considerably larger effective static stiffness, higher resonant frequencies, and moderated Q values [78, 79]. The presence of nodes along the cantilever geometry for the higher flexural modes produces an effective shortening of the cantilever length that manifest in an notable increment of the associated resonant frequency and stiffness. Details about the predicted geometry and parameters of the second and third eigenmodes of a rectangular cantilever with respect to the fundamental mode are summarized in Fig. 3.15.

An open question is whether the equation that relates the frequency shift with the tip–surface interaction force (3.1) still holds to perform force spectroscopy using the cantilever higher flexural modes. Notice that (3.1) is derived under the assumption that a point-mass model correctly describes the dynamics of a continuous cantilever [14, 27, 32]; and this is the case for the first flexural mode, while an appropriate parametrization is required for higher eigenmodes [79].

To confirm the validity of (3.1) for force spectroscopy using higher flexural modes, we have compared force spectroscopic measurements acquired over the same atom and with the same tip–apex termination alternately using the first and second flexural modes of a rectangular cantilever [80]. These results are displayed in Fig. 3.16. We first measured a frequency shift curve over a corner adatom of the Si(111)-(7 $\times$ 7) surface using the fundamental mode, then we retracted the tip from the surface, switch to operation using the

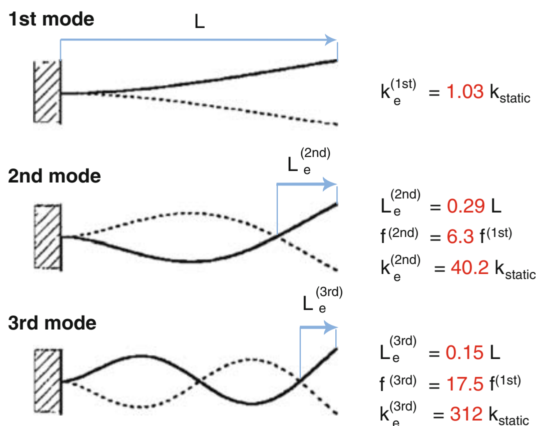

Fig. 3.15. Predicted geometry, effective length, effective static stiffness, and resonant frequency for the first, second, and third flexural modes of a rectangular cantilever, excluding effects associated with the mass and position of the cantilever tip

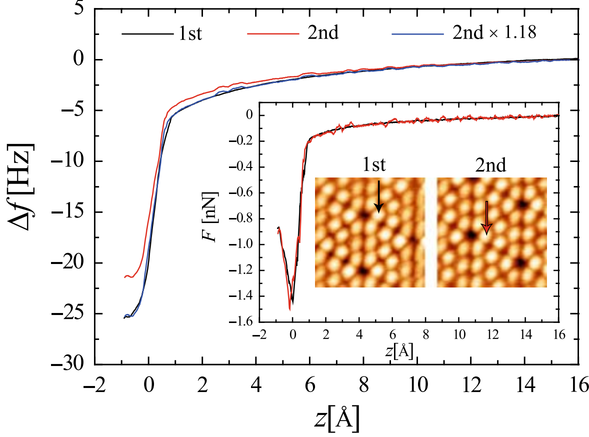

Fig. 3.16. Force spectroscopic measurements performed using the first and second flexural modes of a rectangular cantilever over the same surface atom with an identical tip termination. The *blue curve* corresponds to the frequency shift characteristic measured with the second eigenmode scaled by a 1.18 factor. Acquisition parameters for the first (second) flexural mode were $f_{1(2)} = 157{,}403\ (978{,}904)$ Hz, $k_{\mathrm{s(2nd)}} = 26.9$ (1968) N m^{-1}, and $A_0 = 132$ (28.5) Å. Figure adapted from [80]

second mode, and finally we performed again spectroscopic measurements over the same surface atom using relative large oscillation amplitudes. During the acquisition of these spectroscopic series, the position of the laser spot (located close to the cantilever free end) for the detection of the cantilever dynamics was exactly the same, and the calibration of the oscillation amplitude [24, 38] was independently performed for each flexural mode after concluding the measurements.

Surprisingly, while the ratio of resonant frequencies was in good agreement with the theoretical predictions ($f_2/f_1 = 6.2$) [78, 79], we have found that a scaling of the frequency shift curve obtained with the second mode (Fig. 3.16) leads to an experimental estimation of the equivalent stiffness for the second mode which is 73 ± 17 times larger than that of the first mode, in contrast with a theoretically predicted ratio $k_{\mathrm{2nd}}/k_{\mathrm{1st}} \approx 40.2$. This discrepancy in the $k_{\mathrm{2nd}}/k_{\mathrm{1st}}$ ratio may be attributed to the presence of the tip.

In the inset plot of Fig. 3.16, it is displayed the total tip–surface interaction forces obtained from the frequency shift curves measured with the first and the second flexural mode, respectively. As predicted in [79], the estimation of the equivalent stiffness for the point-mass model associated with the corresponding cantilever eigenmode is sufficient condition to validate (3.1) for force spectroscopy using the cantilever higher eigenmodes. The effective stiffness of higher flexural modes can be estimated by fitting the corresponding thermal noise spectra, and independently evaluating the Q-value of the cantilever oscillation in the corresponding mode.

As it has been stated earlier, the larger equivalent stiffness of the cantilever higher flexural modes enables operation of FM-AFM using small oscillation amplitudes. Driving the cantilever oscillation at the second mode, we have been able to measure force spectroscopic characteristics with oscillation amplitudes as small as 3.6 Å. Interestingly, at such small oscillation amplitudes, the normalized frequency shift [27] does not follow an $A_0^{3/2}$ scaling [13] anymore [38, 80]. This is evidenced in a series of frequency shift curves displayed in Fig. 3.17, and measured using the second flexural mode over the same surface atom with an identical tip–apex termination but at cantilever oscillation amplitudes ranging from 32.7 to 3.6 Å. While all the frequency shift curves provide an identical tip–surface interaction force independently of the oscillation amplitude, the normalized frequency shift (γ) of curves acquired with small amplitudes gradually diverges from the ones measured with larger oscillation amplitudes. The normalized frequency shift scaling fails because the approximation of (3.1) for large oscillation amplitudes [81]

$$\Delta f \approx \frac{f_\mathrm{r}}{\sqrt{2}\pi k_\mathrm{s} A_0^{3/2}} \int_0^\infty \frac{F_\mathrm{int}(z'+x)}{\sqrt{x}}\,\mathrm{d}x$$

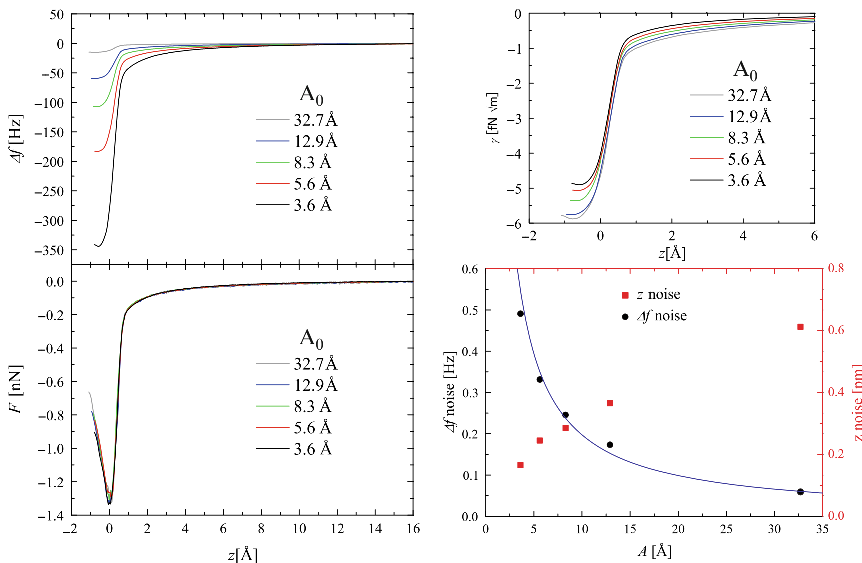

Fig. 3.17. Series of frequency shift curves acquired over the same adatom of a Si(111)-(7 × 7) surface with identical tip–apex termination using the second flexural mode of a rectangular cantilever driven at different oscillation amplitudes. The other panels show the corresponding normalized frequency shift (γ) [27] and tip–surface interaction force curves, as well as the dependence of the frequency shift and tip–sample distance noise with the cantilever oscillation amplitude (in this graph the curve is a A_0^{-1} fit to the frequency shift noise data). Acquisition parameters were $f_2 = 987,155$ Hz and $k_{2\mathrm{nd}} = 2,062\,\mathrm{N\,m^{-1}}$. Figure adapted from [80]

[with $x = A_0(1+u)$ from (3.1)], where the prefactor gives rise to the γ-scaling, does not longer hold. Therefore, comparison of frequency shift values measured with different cantilever oscillation parameters through the normalized frequency shift is not valid for small oscillation amplitudes. Another consequence of this behavior is that the precise calibration of the cantilever oscillation amplitude using the normalized frequency shift method [24, 38, 75] requires setting large enough oscillation amplitudes.

The set of frequency shift curves shown in Fig. 3.17 enables quantifying the improvement in the signal-to-noise ratio associated with the reduction of the cantilever oscillation amplitude. The noise analysis from these curves (see details in [80]) shows a good agreement with theoretical predictions [5, 8, 69]: the noise in the frequency shift increases inversely proportional to the oscillation amplitude, while the noise in the tip–sample distance reduces as the oscillation amplitude becomes smaller (Fig. 3.17). Although the noise in the frequency shift increases, the absolute value of the frequency shift signal obtained at small oscillation amplitudes for an identical tip–surface interaction force is considerably larger than the one measured at bigger oscillation amplitudes, leading to an overall improvement of the signal-to-noise ratio. Thus, operation of FM-AFM at small oscillation amplitudes seems to represent a refinement of sensitivity to tip–surface interaction forces and spatial resolution.

3.7 Summary

In this chapter, we have described examples of how force spectroscopy performed over individual atomic positions provides valuable information about the mechanical properties of the tip–surface interface, and facilitates the possibility of disclosing the chemical composition of a surface at atomic scale. The potential and opportunities offered by force spectroscopy will see a revolution in the near future with the application of this technique to a widen spectrum of surfaces and scientific problems, as well as with an increasing number of groups adapting and further developing the technique. Very promising achievements and an exciting panorama are foreseen with the ability of quantifying forces not only over individual atoms but mapping them over a line [15, 26, 56, 68, 82] or even over a surface area (see Chaps. 2, 5, and 9). Without any doubt, simultaneous measurements of forces and tunneling currents performed at small oscillation amplitudes over atoms, molecules, and nanostructures will bring new and exciting breakthroughs in nanoscience.

Acknowledgments

The authors are very grateful to friends and colleagues who decisively contributed to the works and achievements summarized in this chapter: Masayuki Abe, Pablo Pou, Pavel Jelinek, and Ruben Perez. The authors are specially

grateful to Prof. Seizo Morita for guidance, mentoring, and constant and unconditional support.

References

1. G. Binnig, C.F. Quate, C. Gerber, Phys. Rev. Lett. **56**(9), 930 (1986)
2. F. Giessible, Science **267**, 68 (1995)
3. Y. Sugawara, M. Ohta, H. Ueyama, S. Morita, Science **270**, 1646 (1995)
4. S. Kitamura, M. Iwatsuki, Jpn. J. Appl. Phys. **34**(1B), L145 (1995)
5. T.R. Albrecht, P. Grütter, D. Horne, D. Rugar, J. Appl. Phys. **69**(2), 668 (1991)
6. S. Morita, R. Wiesendanger, E. Meyer, *Noncontact Atomic Force Microscopy*. NanoScience and Technology (Springer, Berlin, 2002)
7. R. García, R. Pérez, Surf. Sci. Rep. **47**(6–8), 197 (2002)
8. F.J. Giessibl, Rev. Mod. Phys. **75**(3), 949 (2003)
9. B. Gotsmann, D. Krüger, H. Fuchs, Europhys. Lett. **239**(2), 153 (1997)
10. B. Gotsmann, B. Anczykowski, C. Seidel, H. Fuchs, Appl. Surf. Sci. **140**, 314 (1999)
11. B. Gotsmann, C. Seidel, B. Anczykowski, H. Fuchs, Phys. Rev. B **60**(15), 11051 (1999)
12. H. Hölscher, W. Allers, A. Schwarz, U.D. Schwarz, R. Wiesendanger, Phys. Rev. Lett. **83**(23), 4780 (2003)
13. H. Hölscher, A. Schwarz, W. Allers, U.D. Schwarz, R. Wiesendanger, Phys. Rev. B **61**(19), 12678 (2000)
14. H. Hölscher, B. Gotsmann, W. Allers, U.D. Schwarz, H. Fuchs, R. Wiesendanger, Phys. Rev. B **64**(7), 075402 (2001)
15. H. Hölscher, S.M. Langkat, A. Schwarz, R. Wiesendanger, Appl. Phys. Lett. **81**(23), 4428 (2002)
16. M.A. Lantz, H.J. Hug, R. Hoffmann, P.J.A. van Schendel, P. Kappenberger, S. Martin, A. Baratoff, H.J. Güntherodt, Science **291**(5513), 2580 (2001)
17. R. Pérez, M. Payne, I. Štich, K. Terakura, Phys. Rev. Lett. **78**(4), 678 (1997)
18. R. Pérez, I. Štich, M. Payne, K. Terakura, Phys. Rev. B **58**(16), 10835 (1998)
19. A.I. Livshits, A.L. Shluger, A.L. Rohl, A.S. Foster, Phys. Rev. B **59**(3), 2436 (1999)
20. A.S.U. Kaiser, R. Wiesendanger, **446**, 522 (2007)
21. R. Bennewitz, M. Bammerlin, M. Guggisberg, C. Loppacher, A. Baratoff, E. Meyer, H.J. Güntherodt, Surf. Interface Anal. **27**, 462 (1999)
22. M. Guggisberg, M. Bammerlin, C. Loppacher, O. Pfeiffer, A. Abdurixit, V. Barwich, R. Bennewitz, A. Baratoff, E. Meyer, H.J. Güntherodt, Phys. Rev. B **61**(16), 11151 (2000)
23. N. Suehira, Y. Tomiyoshi, Y. Sugawara, S. Morita, Rev. Sci. Instrum. **72**(7), 2971 (2001)
24. M. Abe, Y. Sugimoto, O. Custance, S. Morita, Appl. Phys. Lett. **87**(17), 173503 (2005)
25. M. Abe, Y. Sugimoto, O. Custance, S. Morita, Nanotechnology **16**(12), 3029 (2005)
26. M. Abe, Y. Sugimoto, T. Namikawa, K. Morita, N. Oyabu, S. Morita, Appl. Phys. Lett. **90**(20), 203103 (2007)
27. F.J. Giessibl, Phys. Rev. B **56**(24), 16010 (1997)

28. U. Dürig, Appl. Phys. Lett. **76**(9), 1203 (2000)
29. F.J. Giessibl, Appl. Phys. Lett. **78**(1), 123 (2001)
30. F.J. Giessibl, H. Bielefeldt, S. Hembacher, J. Mannhart, Ann. Phys. (Leipzig) **10**(11–12), 887 (2001)
31. J.E. Sader, S.P. Jarvis, Appl. Phys. Lett. **84**(10), 1801 (2004)
32. U. Dürig, Appl. Phys. Lett. **75**(3), 433 (1999)
33. R. Hoffmann, A. Baratoff, H.J. Hug, H.R. Hidber, H. v Löhneysen, H.J. Güntherodt, Nanotechnology **18**(39), 395503 (2007)
34. Y. Sugimoto, P. Jelinek, P. Pou, M. Abe, S. Morita, R. Pérez, O. Custance, Phys. Rev. Lett. **98**(10), 106104 (2007)
35. R. Hoffmann, L.N. Kantorovich, A. Baratoff, H.J. Hug, H.J. Güntherodt, Phys. Rev. Lett. **92**(14), 146103 (2004)
36. Y. Sugimoto, P. Pou, O. Custance, P. Jelinek, S. Morita, R. Pérez, M. Abe, Phys. Rev. B **73**(20), 205329 (2006)
37. J.P. Cleveland, S. Manne, D. Bocek, P.K. Hansma, Rev. Sci. Instrum. **64**(2), 403 (1993)
38. G. Simon, M. Heyde, H.P. Rust, Nanotechnology **18**, 255503 (2007)
39. N. Oyabu, P. Pou, Y. Sugimoto, P. Jelinek, M. Abe, S. Morita, R. Pérez, O. Custance, Phys. Rev. Lett. **96**(10), 106101 (2006)
40. J.P. Cleveland, B. Anczykowski, A.E. Schmid, V.B. Elings, Appl. Phys. Lett. **72**(20), 2613 (1998)
41. C. Loppacher, R. Bennewitz, O. Pfeiffer, M. Guggisberg, M. Bammerlin, S. Schär, V. Barwich, A. Baratoff, E. Meyer, Phys. Rev. B **62**(20), 13674 (2000)
42. R. Bennewitz, A.S. Foster, L.N. Kantorovich, M. Bammerlin, C. Loppacher, S. Schär, M. Guggisberg, E. Meyer, A.L. Shluger, Phys. Rev. B **62**(3), 2074 (2000)
43. M. Gauthier, R. Perez, T. Arai, M. Tomitori, T. M, PRL **89**(14), 146104 (2002)
44. R.S. Becker, B.S. Swartzentruber, J.S. Vickers, T. Klitsner, Phys. Rev. B **39**, 1633 (1989)
45. N. Takeuchi, A. Selloni, E. Tosatti, Phys. Rev. Lett. **69**, 648 (1992)
46. M. Abe, Y. Sugimoto, S. Morita, Nanotechnology **16**(3), S68 (2005)
47. H.J. Güntherodt, E.M. D. Anselmetti, *Forces in Scanning Probe Methods*, *NATO ASI, Ser. E*, vol. 286 (Kluwer, Dordrechet, 1995)
48. N. Sasaki, M. Tsukada, Jpn. J. Appl. Phys. **39**(12B), L1334 (2000)
49. L.N. Kantorovich, T. Trevethan, Phys. Rev. Lett. **93**(23), 236102 (2004)
50. N. Oyabu, O. Custance, I. Yi, Y. Sugawara, S. Morita, Phys. Rev. Lett. **90**(17), 176102 (2003)
51. Y. Sugimoto, P. Pou, O. Custance, P. Jelinek, M. Abe, R. Pérez, S. Morita, Science **322**, 413 (2008)
52. M.A. Lantz, H.J. Hug, P.J.A. van Schendel, R. Hoffmann, S. Martin, A. Baratoff, A. Abdurixit, H.J. Güntherodt, C. Gerber, Phys. Rev. Lett. **84**(12), 2642 (2000)
53. B.C. Stipe, M.A. Rezaei, W. Ho, Phys. Rev. Lett. **79**(22), 4397 (1997)
54. H.J. Hug, A. Baratoff, *Noncontact Atomic Force Microscopy* (Springer, Berlin, 2002), chap. 20, pp. 395–432
55. S.A. Ghasemi, S. Goedecker, A. Baratoff, T. Lenosky, E. Meyer, H.J. Hug, Phys. Rev. Lett. **100**(23), 236106 (2008)
56. A. Schirmeisen, D. Weiner, H. Fuchs, Phys. Rev. Lett. **97**(13), 136101 (2006)
57. W. Kamiński, P. Jelinek, R. Pérez, F. Flores, J. Ortega, Appl. Surf. Sci. **234**, 286 (2004)

58. S.T. Jemander, N. Lin, H.M. Zhang, R.I.G. Uhrberg, G.V. Hansson, Surf. Sci. **475**, 181 (2001)
59. P. Dieska, I. Štich, R. Pérez, Phys. Rev. Lett. **95**(12), 126103 (2005)
60. S.H. Ke, T. Uda, I. Štich, K. Terakura, Phys. Rev. B **63**(24), 245323 (2001)
61. A. Charrier, R. Pérez, F. Thibaudau, J.M. Debever, J. Ortega, F. Flores, J.M. Themlin, Phys. Rev. B **64**(11), 115407 (2001)
62. Y. Sugimoto, P. Pou, M. Abe, P. Jelinek, R. Pérez, S. Morita, O. Custance, Nature **445**, 64 (2007)
63. L. Pauling, *The Nature of the Chemical Bond*, 3rd edn. (Cornell University Press, New York, 1960)
64. V. Caciuc, H. Hölscher, S. Blügel, H. Fuchs, Phys. Rev. Lett. **96**(1), 016101 (2006)
65. S.H. Ke, T. Uda, R. Pérez, I. Štich, K. Terakura, Phys. Rev. B **60**(16), 11631 (1999)
66. S. Hembacher, F.J. Giessibl, J. Mannhart, Science **305**(5682), 380 (2004)
67. Y. Sugimoto, M. Abe, S. Hirayama, N. Oyabu, O. Custance, S. Morita, Nat. Mater. **4**(2), 156 (2005)
68. M. Ternes, C. Lutz, C. Hirjibehedin, F. Giessibl, A. Heinrich, **319**(5866), 1066 (2008)
69. F.J. Giessibl, H. Bielefeldt, S. Hembacher, J. Mannhart, Appl. Surf. Sci. **140**, 352 (1999)
70. F.J. Giessibl, H. Bielefeldt, Phys. Rev. B **61**(15), 9968 (2000)
71. F.J. Giessibl, S. Hembacher, M. Herz, C. Schiller, J. Mannhart, Nanotechnology **15**, S79 (2004)
72. J.L. Yanga, M. Despontb, U. Drechsler, B.W. Hoogenboom, P.L.T.M. Frederix, S. Martin, A. Engel, P. Vettiger, H.J. Hug, Appl. Phys. Lett. **86**(13), 134101 (2005)
73. B.W. Hoogenboom, P.L.T.M. Frederix, J.L. Yang, S. Martin, Y. Pellmont, M. Steinacher, S. Zäch, E. Langenbach, H.J. Heimbeck, A. Engel, H.J. Hug, Appl. Phys. Lett. **86**(7), 074101 (2005)
74. F.J. Giessibl, Appl. Phys. Lett. **73**(26), 3956 (1998)
75. F.J. Giessibl, Appl. Phys. Lett. **76**(11), 1470 (2000)
76. S. Kawai, S. Kitamura, D. Kobayashi, S. Meguro, H. Kawakatsu, Appl. Phys. Lett. **86**(19), 193107 (2005)
77. S.Kawai, H. Kawakatsu, Appl. Phys. Lett. **88**(13), 133103 (2006)
78. S. Rast, C. Wattinger, U. Gysin, E. Meyer, Rev. Sci. Instrum. **71**(7), 2772 (2000)
79. J. Melcher, S. Hu, A. Raman, Appl. Phys. Lett. **91**(5), 053101 (2007)
80. Y. Sugimoto, S. Innami, M. Abe, O. Custance, S. Morita, Appl. Phys. Lett. **91**(9), 093120 (2007)
81. H. Hölscher, B. Gotsmann, A. Schirmeisen, Phys. Rev. B **68**(15), 153401 (2003)
82. Y. Sugimoto, T. Namikawa, K. Miki, M. Abe, S. Morita, Phys. Rev. B **77**(19), 195424 (2008)